2022

Feasibility Study on Emission Line Spectroscopy Between 350 Nm and 750 Nm Of Runaway Star Bow Shocks in the Milky Way Using Currently Operating Observatories with Open Submission Policies

John Scheele
Minnesota State University, Mankato

Feasibility study on emission line spectroscopy between 350 nm and 750 nm of runaway star bow shocks in the Milky Way using currently operating observatories with open submission policies

John Scheele

A thesis submitted in partial fulfillment of the

requirements for the degree of

Masters of Science

in

Physics

at Minnesota State University, Mankato

Minnesota State University, Mankato

Mankato, Minnesota

Spring 2022

2022/4/18

Feasibility study on emission line spectroscopy between 350 nm and 750 nm of runaway star bow shocks in the Milky Way using currently operating observatories with open submission policies

John Scheele

This thesis has been examined and approved by the following members of the student's committee.

Paul Eskridge, PhD

Michael Rutkowski, PhD

Thomas Brown, PhD

Contents

Feasibility study on emission line spectroscopy between 350 nm and 750 nm of runaway star bow shocks in the Milky Way using currently operating observatories with open submission policies

John Scheele

A THESIS SUBMITTED IN PARTIAL FULFILLMENT OF THE

REQUIREMENTS FOR THE DEGREE OF

Masters of Science in Physics

MINNESOTA STATE UNIVERSITY, MANKATO

MANKATO, MINNESOTA

April, 2022

ABSTRACT

Numerous runaway stars with bow shocks have been observed distributed around the Galaxy. These shocks have previously been observed in the infrared, $H\alpha$, $[OIII]$, and $[NII]$ lines. Recently hydrodynamic simulations allow for theoretical emissions of a runway star bow shock to be calculated. Expanding on these simulations shows that simultaneous observations in visible spectrum for $H\alpha$, $HeI\lambda 5876$Å, and $[OIII]$ by the GMOS instruments of the Gemini Observatories are possible, allowing direct composition measurements of the ISM in the Milky Way Galaxy.

1. INTRODUCTION

Hydrodynamic simulations of runway stars allow us to gain unprecedented insights into the underlying physics and composition of their bow shocks and the surrounding ISM in the Milky Way Galaxy (MW).

Runaway stars are differentiated from the numerous surrounding stars by the difference in their translational (or peculiar) velocity to the local mean. The peculiar velocity of these stars is omnidirectional, not just in the direction of travel for the local group (Brown 2015). Simultaneously, their peculiar velocity is faster then the speed of sound for the local ISM Comeron & Kaper (1998). A star that meets these two definitions is classified as a runaway star.

Runaway stars traveling through the MW have been observed to generate bow shocks by the collision of their stellar wind with the surrounding ISM at supersonic velocities (Wilkin 1996). These shocks have been observed in numerous wavelengths over the decades. Some of the earliest observations of bow shocks were done in $H\alpha$, $[OIII]$, and $[NII]$ by Gull & Sofia (1979). A later survey by Brown & Bomans (2005) examined the emission of eight unique bow shocks in $H\alpha$. More recent observations have been analyzed from images taken by the Wide-Field Infrared Survey Explorer (WISE) by Kobulnicky et al. (2016), and others have found numerous bow shocks around runaway stars.

These observations have motivated theoretical analysis on the structure and formation of a runaway star bow shock. Wilkin (1996) looks at the relation between the mass loss rate of a star ($\dot{M}$), its peculiar velocity (v_*), the ISM density (ρ_{ISM}), and the distance the shock front (standoff distance) is from the star ($R(0)$). Simulations by

Comeron & Kaper (1998) utilized the Euler equations of hydrodynamics in a computational grid to run numerical simulations of runaway star bow shocks. Recently Meyer et al. (2016) has shown that bow shocks simulations can be used to calculate the observable luminosity of the $H\alpha$, and $[OIII]$ lines for a variety of different star masses, velocities and ISM densities. This is further expanded on in Meyer et al. (2021), where the bow shock of Betelgeuse is simulated using 3D Magnetohydrodynamics.

Some runway stars are classified as hyper velocity stars depending both on how they obtained their peculiar velocity, and its magnitude (Brown 2015). A hyper velocity star (HVS) is generated by interaction between a multiple star system and a supermassive black hole (Brown 2015) in the center of the MW. The initial v_* from this method exceeds the galactic escape velocity of 1000 km/s (Brown 2015). Runaway stars have two primary origin methods including gravitational interaction (Poveda et al. 1967) and binary supernovae (Blaauw 1961). These methods can occur throughout the MW, leading to a large distribution of runway stars (Kobulnicky et al. 2016), whereas most hyper velocity stars are only found close to the Galactic Center (Brown 2015). Since HVS are located much further away from Earth, we will restrict our simulations to runaway star bow shocks.

The composition of the ISM has been observed indirectly in the past through looking at absorption lines [1]. To date though it is very difficult to make direct observations of the ISM composition[2]. Only 2 spacecraft launched from earth have reached interstellar space, Voyagers 1 and 2, and neither has a way to directly measure the ISM

[1] https://www.cosmos.esa.int/documents/1866264/3219248/Wimmer-SchweingruberR_2019-08-04-interstellar-whitepaper.pdf

[2] see 1

composition[3]. This lack of direct observations make bow shocks appealing spectroscopy targets, because the shocks are comprised of the ISM and not the stars stellar wind (Wilkin 1996), they could provide a unique opportunity to directly observe the ISM composition in multiple locations around the MW.

Simulating runaway star bow shocks using the open source hydrodynamics code, PLUTO, (Mignone et al. 2007) allows us to further expand on the work of Meyer et al. (2016) and determine the observability of bow shocks in the $HeI\,\lambda$5876Å emission band by the Gemini Observatories GMOS instruments.

[3] https://voyager.jpl.nasa.gov/mission/status/

2. METHODOLOGY

2.1. *Hydrodynamics*

The simulations are governed by the Euler equations for hydrodynamics. These three conservation equations are solved by the PLUTO code by Mignone et al. (2007), and take into account the relevant physics of the bow shock. For a more complete explanation of the equations see Meyer et al. (2014) and Mignone et al. (2007).

The hydrodynamic equations are identical to those used by Meyer et al. (2014) and are outlined below.

$$\frac{\partial \rho}{\partial t} + \nabla \cdot (\rho \mathbf{v}) = 0 \tag{1}$$

$$\frac{\partial \rho \mathbf{v}}{\partial t} + \nabla \cdot (\mathbf{v} \otimes \rho \mathbf{v} + \nabla p) = \mathbf{0} \tag{2}$$

$$\frac{\partial E}{\partial t} + \nabla \cdot (E\mathbf{v}) + \nabla \cdot (\rho \mathbf{v}) = \Phi(T, \rho) + \nabla \cdot \mathbf{F_c} \tag{3}$$

Equation 1 - 3 are the three conservation equations where $\mathbf{v}$ is the gas velocity, ρ is the density, p is the pressure, E is the energy, and T is the temperature of the gas (Meyer et al. 2014). Equation 1 is also known as the mass-conservation equation (Batchelor 2000), where the change in density for the gas is opposite to the change in its velocity (Batchelor 2000). Equation 2 accounts for momentum conservation for the gas, and Equation 3 handles energy conservation.

Furthermore, the total energy density in the gas is given by equation 4, below (Meyer et al. 2014).

$$E = \frac{p}{(\gamma - 1)} + \frac{\rho v^2}{2} \tag{4}$$

Equation 4 shows how the gas' energy is equal to the sum of its thermal and kinetic energy. Equation 4 is also the ideal gas law in another form. The factor γ is adiabatic index of the gas (Meyer et al. 2014).

Assuming an ideal gas, we can obtain the gas temperature directly by solving the ideal gas law for T.

$$T = \mu \frac{m_H p}{k_B \rho} \tag{5}$$

where μ is the mean molecular mass, m_H is the mass of a hydrogen atom, p is the pressure, k_B is Boltzmann's constant, and ρ is the density of the gas.

As a runaway star travels through interstellar space, the stellar wind, and surrounding ISM undergo both heating and cooling from various interactions. To accurately calculate the change in temperature for each time step, we need to look at the heating and cooling effects on the gas. These effects are included in Equation 6.

$$\Phi(T, \rho) = n_H^2 \Gamma_{Heat}(T) - n_H^2 \Lambda(T) \tag{6}$$

Equation 6 allows us to look at the heating (Γ_{Heat}) and the optically thin cooling (Λ) of the bow shock.

To fully implement cooling and heating we need to find n_H, by solving $\rho = \mu n m_H$ of the gas for n. Doing so gives us Equation 7:

$$n_H = \frac{\rho}{\mu m_H} \tag{7}$$

Combining equations 6 and 7 allows us to find the cooling rate for each grid space at a given temperature T. We can find the sound speed of the gas (c_s)using Equation 10-6 from Spitzer (1978) and solving for C_s.

$$c_s = \sqrt{\frac{\gamma p}{\rho}} \tag{8}$$

2.2. *Runaway Stars*

For a star to be classified as a runaway its peculiar velocity must exceed the ISM sound speed calculated with Equation 8 (Comeron & Kaper 1998). The peculiar velocity of a star, (v_*), is determined by differencing its velocity with the local mean. When a star is moving at these speeds, it is possible for a bow-shock to form ahead of the star in the direction of travel (Comeron & Kaper 1998). For each star, this minium velocity is dependent on the properties of the local ISM, ()see Equation 8). For this paper, we will use the 10.0 km/s minimum peculiar velocity in the simulations of Meyer et al. (2014) as the cutoff velocity of a star to be simulated.

Two primary progenitor scenarios produce runaway stars: binary-supernova (Blaauw 1961), and dynamical ejection scenario (Poveda et al. 1967), both of which have been identified in the MW (Hoogerwerf et al. 2000). The particular progenitor scenario for a runaway star can be inferred using spatial position data from astronomical surveys in order to calculate the past orbital locations of both the runaway star and the region it came from (Hoogerwerf et al. 2001). An outline of each method along with their key characteristics can be found below.

In the binary supernova scenario of Blaauw (1961), the runaway star is ejected from its binary system by gravitational instability, when its larger mass primary explodes as a type II supernova. When M_1 explodes as a supernova, the total kinetic energy of the

system $< KE >$ stays the same, while the required orbital velocity $v_{orbital}$ decreases. This causes the ejection of M_2 as a runaway star with a velocity comparable to its pre-explosion orbital velocity. M_1 is then either a black hole or neutron star (Hoogerwerf et al. 2001).

this is in contrast to the dynamical ejection scenario of Poveda et al. (1967), where the runway star originates from gravitational interactions between stars in dense, compact clusters. Hoogerwerf et al. (2001) outlines the two-binary star encounter as the primary progenitor method for gravitational interactions. Here, two binary systems that approach sufficiently close to each other can produce four distinct results: two separate binary systems, a single star and a triple star system, two stars and a binary, or four individual unbound stars. The most likely result of the interaction however, has been shown to be the third scenario: two unbound stars and a binary (Hoogerwerf et al. 2001).

2.3. *Bow Shocks*

In Figure 1, the general structure of a bow shock illustrated.

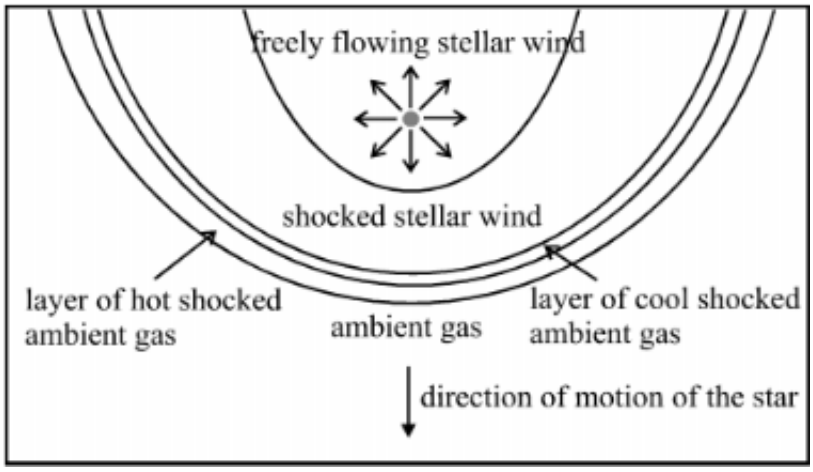

Figure 1. Bow shock structure overview from Comeron & Kaper (1998)

Here, the key physical regions of a bow shock are presented: the stellar wind out flowing from the progenitor star, the region of shocked stellar wind, and the hot and cool layers of the ambient ISM gas associated with the shocked region itself (Comeron & Kaper 1998). $R(0)$ is the distance from the star to the shocked ISM, and varies depending on the stars parameters. The shocked ISM regions are the most luminous part of the shock, while the thinnest part of the shock is along the direction of v_*.

In the instantaneous cooling approximation of Wilkin (1996), a bow shock is assumed to form at a distance $R(0)$ away from the star. The equation for the standoff distance R(0) of a bow shock.

$$R(0) = \sqrt{\frac{\dot{M} v_w}{4\pi \rho_{ISM} v_*^2}} \tag{9}$$

Here $\dot{M}$ is the mass loss rate for the star, v_w is the velocity of the stellar wind, ρ_{ISM} is the ISM density around the star, and v_* is the stars peculiar velocity (Meyer et al. 2014).

In our numerical simulations, though, we use a time-stepped cooling function which is a more accurate representation of cooling than the instantaneous method of Wilkin (1996) (Comeron & Kaper 1998). In this case there will be a high temperature (but low density layer) of gas between the bow shock and the star, which can cause the bow shock to start further out than the $R(0)$ approximation of Wilkin (1996) (Comeron & Kaper 1998). While Equation 9 is not solved numerically in our simulations it does play a key role in the setup of each simulation. Equation 9 shows that the key underlying factors determining the $R(0)$ are $\dot{M}$ and ρ_{ISM}. Both the velocity of the star and stellar wind are much lower then the preceding terms and will have less of an effect on the standoff distance,as we will see later.

The density of the stellar wind is found using Equation 10 below (Meyer et al. 2014).

$$\rho_w = \frac{\dot{M}}{4\pi r^2 v_w} \tag{10}$$

In Equation 10, we see that the density ρ_w is mainly determined by $\dot{M}$, and the distance from the star. While Equation 9 is used as a reference in setting up our simulations, Equation 10 is solved at each time step to determine ρ_w around the star. v_w can be calculated using the method of Eldridge et al. (2006). We combine equations 1 and 2 of Eldridge et al. (2006) to form equation 11 below for v_w.

$$v_w = 2\beta_w GM_* \left(\frac{1-\Gamma_w}{R_*}\right) \tag{11}$$

The value of β_w comes from Table 1 of Eldridge et al. (2006), while R_* and M_* are the radius and mass of the star respectively. With Γ_w defined as $\Gamma_w = L_*/L_{edd}$ (Eldridge

et al. 2006). L_{edd} balances the radiation pressure and gravity of a star, and restricts the maximum mass a star can have.

To determine if the ISM around the star is photo-ionized we calculate the Strömgren radius R_S for the star, using Equation 12 below.

$$R_S = \left(\frac{3S_*}{4\pi n^2 \alpha_{rr}^B} \right)^{1/3} \tag{12}$$

Here, α_{rr}^B is the case B recombination rate from Hummer (1994) and S_* as the flux of hydrogen ionizing photons from the star (Meyer et al. 2014). Since the Strömgren radius is larger than the bow shock standoff distance R(0) for O stars, we treat both the stellar wind and ISM as fully ionized (Meyer et al. 2014). A more thorough overview of runaway star bow shocks can be found in the papers by Wilkin (1996), Comeron & Kaper (1998), Mohamed et al. (2012), and Meyer et al. (2014).

For each of the simulations we need to know t_{cross}, which is how long it takes the star to travel the distance $R(0)$. To find t_{cross} we use Equation 13 below (Meyer et al. 2014).

$$t_{cross} = \frac{R(0)}{v_*} \tag{13}$$

This value allows us to set the run time for our simulations to be long enough to cancel out any numerical artifacts. We will discuss t_{cross} more in the next chapter.

2.4. *Runaway Star Selection*

Ideally, we would like to simulate the emission lines for every known runaway star, but there are $N_s > 709$ runway stars (Kobulnicky et al. 2016). Therefore, it would take a long time to calculate the emissions lines for each one. So we identify a representative

sample size of stars with observations, that can be extrapolated to accurately represent the larger population of runaway stars emission lines. Then we can interpolate our results for stars with properties similar to those that we simulated to determine the feasibility of accurate observations.

We define our initial selection criteria as follows: O stars within 6000 parsecs of Earth, a v_* greater than $10\,km\,s^{-1}$, and a bow shock that is distinct from its progenitor star. The online catalog of Kobulnicky et al. (2016) gives a detailed table of 709 possible runaway stars with bow shocks that are within 6000 parsecs of Earth. In Figure 2, below, the distribution of these runaway stars in the MW from Kobulnicky et al. (2016) is illustrated.

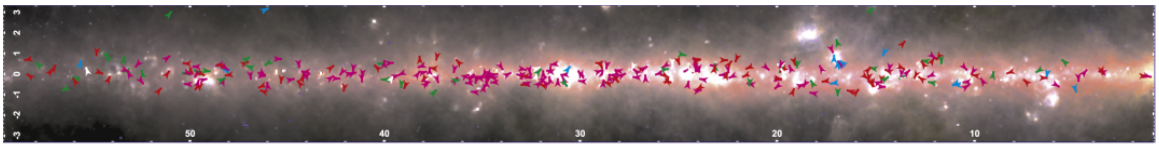

(a)

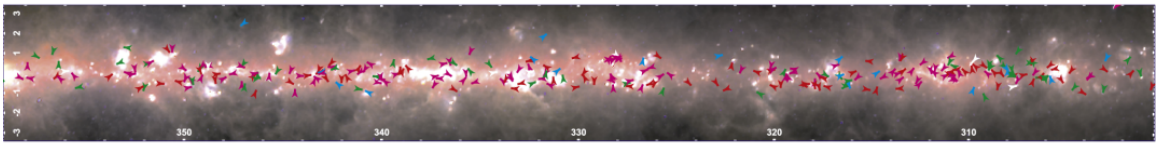

(b)

Figure 2. Locations of bow shock candidates drawn as arrows to indicate the morphological orientation of the nebula. The upper panel shows a portion of the Plane at $0° < t < 60°$, while the lower panel shows the $300° < t < 360°$ region. The colors represent extinction values from the $H - 4.5\,\mu m$ color excess (Kobulnicky et al. 2016)

It is apparent from Figure 2 that the runway stars in the MW are primarily located in the galactic plane. Runway stars are also isotropic in v_*, and have random directions of

travel in the galactic plane. Therefore the direction of travel for runaway star viewed from Earth will not be perpendicular to the direction of v_*.

2.5. *Runaway Stars Selected*

The Kobulnicky et al. (2016) catalog includes very few of the parameters necessary for our simulations and the sample size is too large to effectively simulate. But, Kobulnicky et al. (2018a) and Kobulnicky et al. (2019a), help to refine our sample of runaway stars. Kobulnicky et al. (2018a) outlines a process that utilizes a few steps to calculate $\dot{M}$ for 70 O and early B stars. They start with the momentum flux balancing equation below.

$$\rho_w v_w^2 = \rho_a v_a^2 \tag{14}$$

In Equation 14, ρ_a and v_a are the density of the ISM and peculiar velocity of the star respectively. Kobulnicky et al. (2018a)'s process continues by showing how to find $\dot{M}$ in terms of observable parameters. This is done by combining Eq 10 with Eq 14, substituting $R(0)$ for r and solving for $\dot{M}$ we get Eq 15 for the mass loss rate in terms of observable parameters.

$$\dot{M} = \frac{4\pi R(0)^2 v_a^2 \rho_a}{v_w} \tag{15}$$

Here. v_a is the peculiar velocity of the star, and ρ_a is the ambient ISM density around the star. Kobulnicky et al. (2018a) then calculates $R(0)$ from angular measurements of the standoff distance of the bow shock with other observable parameters, to find the mass loss rate of a star. This is a big shortcoming of Kobulnicky et al. (2018a) method,

as the final equation does not take into account the angle between v_* and the local ISM velocity (v_{ISM}). To compensate fom this shortcoming we will use the 3σ minimum $\dot{M}$ for each selected star in our simulations.

Many of the stars listed in the catalog of Kobulnicky et al. (2019b) have similar M_* and $\dot{M}$. Thus, we can further refine our simulation sample to stars with unique masses. These stars presented also are within the range of M_* simulated by Meyer et al. (2014). By selecting a range of stars with masses similar to those simulated by Meyer et al. (2014) we can verify our simulations by direct comparison. Our final refinement of selection parameters comes from the results of Meyer et al. (2014), seen in Figure 3 below.

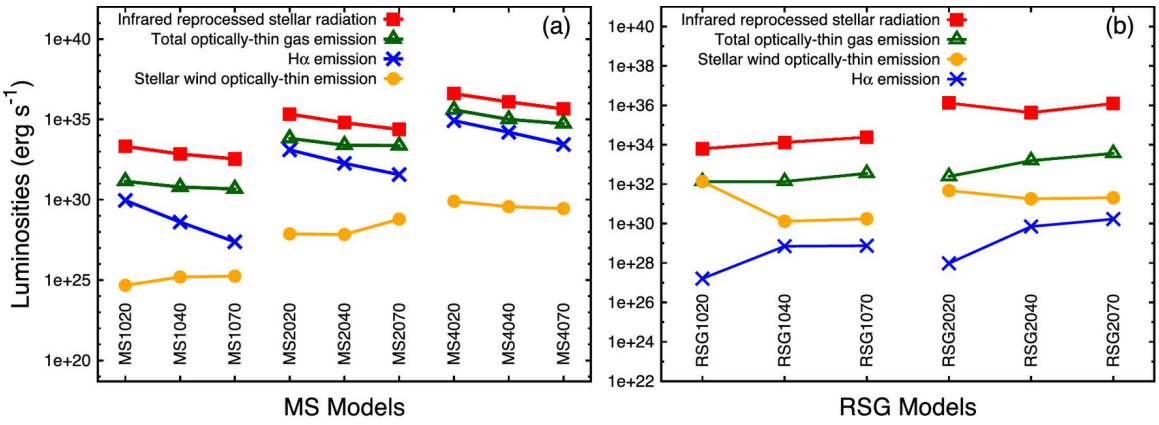

Figure 3. Figure 13 from Meyer et al. (2014). The bow shock luminosities from Meyer et al. (2014) for the main sequence (MS) and red supergiant (RSG) models. The identifiers list the simulation properties in three parts: MS or RSG for the current evolutionary state, the mass in $M_\odot$, and the velocity in km/s. The MS2070 designation is then: a main sequence star, with 20 solar mass, traveling at 70 km/s.

Figure 3, shows that the mass of a runaway star is much more important in determining the luminosity of a bow shock than v_*. This allowed us to focus on a single parameter when selecting our sample size. Thus, we emphasized a mass range between $20M_\odot$ to $60M_\odot$ for our star selection rather than velocity. The selected stars from Kobulnicky et al. (2019b) are outlined in Table 1 below.

Table 1. Selected Stars

Star Name	Spectral Class	Mass	Distance	R(0)
		$M_\odot$	Pc	Pc
G000.1169-00.5703	O8V	26.0	2441	0.344
ζ Ophiuchi	O9.2IV	19.0	112	0.179
KGK 2010-10	O8V	22.0	2115	0.113
CPR 2002A37	O5V	37.0	1703	0.636
BD+43 3654	O4If	58.0	1577	1.623
G342.5873+00.1600	O6V	32.0	3197	0.529

NOTE— Selected stars from Kobulnicky et al. (2019b). Each star is listed with it's name, spectral class, $M\odot$, distance from Sun, and R(0).

Table 1 presents a some key details of the selected stars. Each is a MS O star except BD+43 3654 and ζ Ophiuchi. We chose BD+43 3654 so that our sample would have a larger range of M_*, and its large $R(0)$. ζ Ophiuchi is included because it is the nearest runaway star in Kobulnicky et al. (2019b).

2.6. *Runaway Star Distribution*

We created four 2D visual representations of the stars in Kobulnicky et al. (2019b), using three parameters: Galactic Longitude, Galactic Latitude, and distance from the Sun. These values were then plotted using python to create Cartesian and Polar distribution plots of runaway stars. By looking at the distributions of runaway stars in 2D we are able to present a clearer understanding of how they are distributed relative to the Sun and galactic center than a 3D plot would allow. The position of each star with respect to the Sun is illustrated in Figure 4.

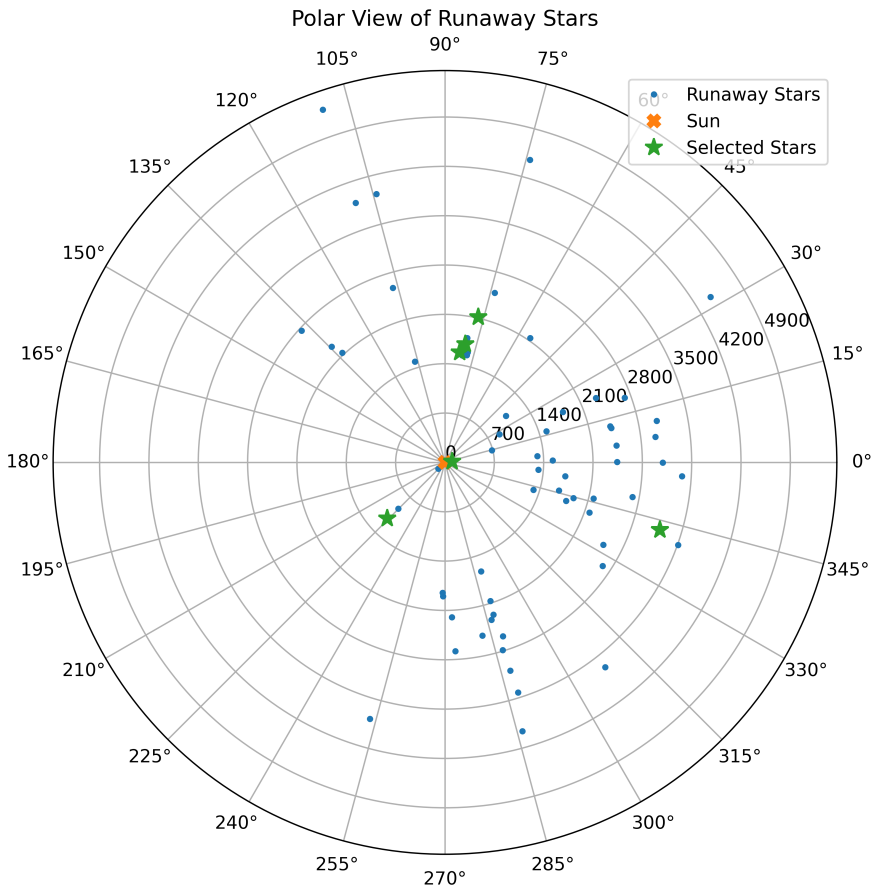

Figure 4. Polar view of runaway stars with the solar system at the origin. The distance increment is in parsecs and angles in galactic longitude with 0° corresponding to galactic center

In Figure 4 the 0° point in azimuth of the arc points in the direction of Galactic Center. The stars in Kobulnicky et al. (2019b) are distributed approximately 180 degrees arc around the Sun. Each selected star is highlighted to show their distribution relative

to other stars in the data set. In Figure 5, we illustrate the position of our selected stars with Galactic Center at the origin.

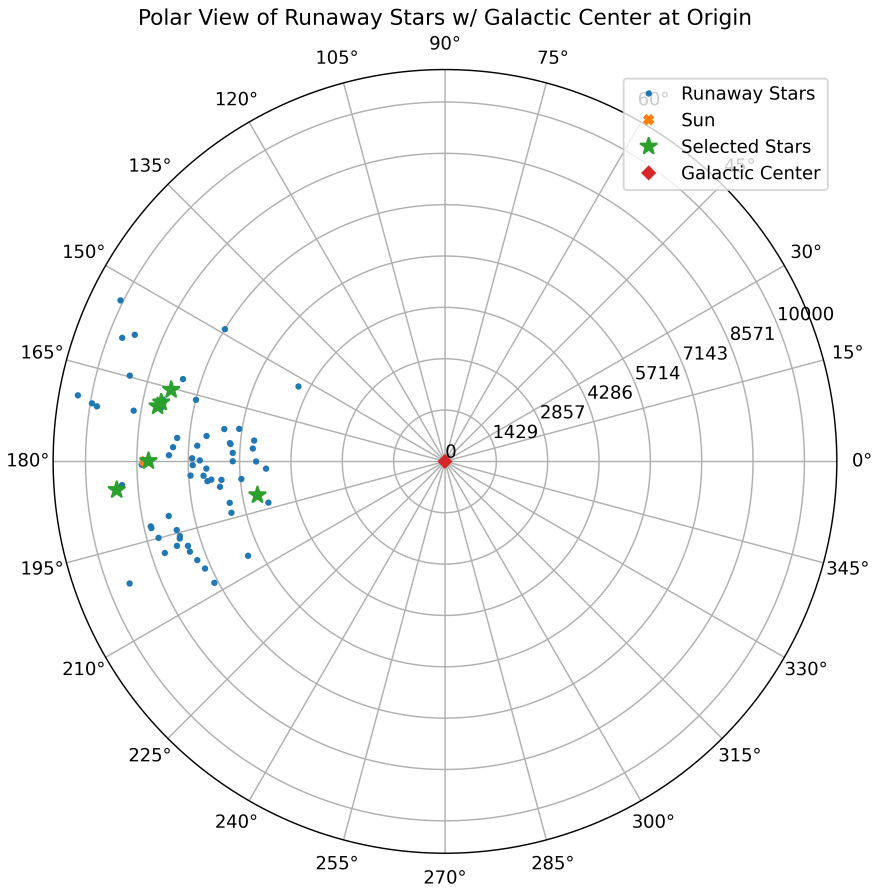

Figure 5. Polar View of runaway stars with Galactic center at the origin. The distance increment is in parsecs and angles in galactic longitude with 0° corresponding to galactic center

In Figure 5, the plot has been shifted to show the positions of each star relative to the center of the MW. While the number of stars in Kobulnicky et al. (2019b) require us to

select a representative sample size, they occupy only a fraction of the galactic disk. We can infer then that the number of runaway stars is much higher than those found in Kobulnicky et al. (2019b) and Kobulnicky et al. (2016). To compliment the two polar plots, we present the edge on view of each stars location relative the Sun in Figure 6

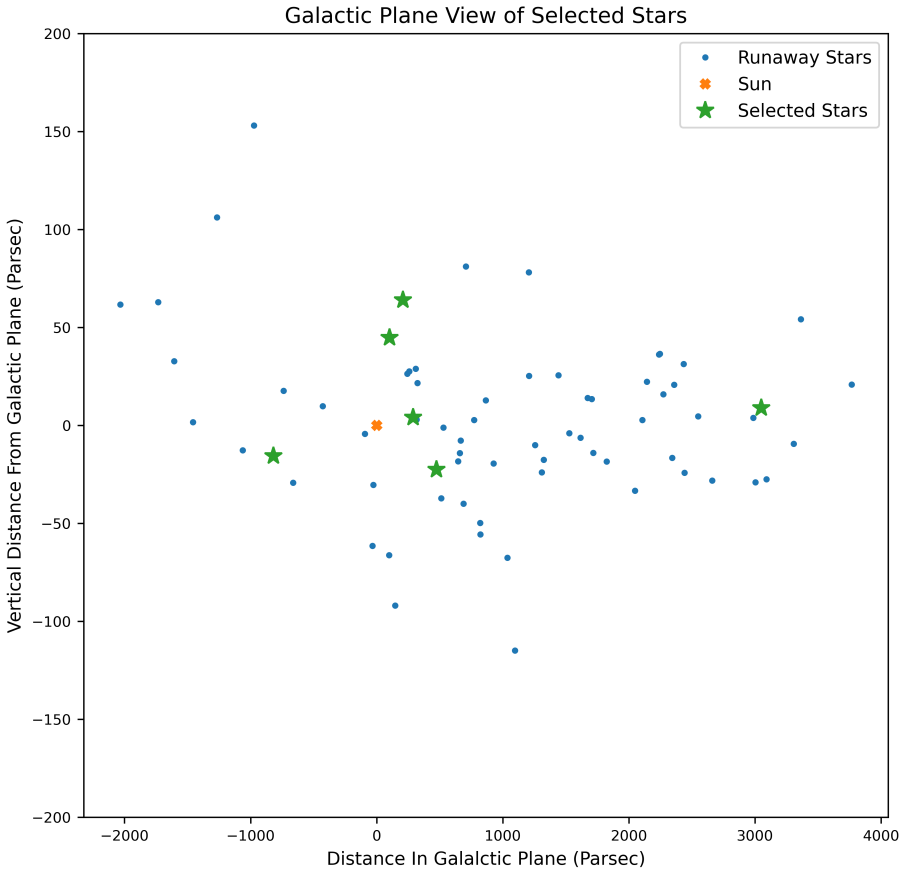

Figure 6. Galactic Plane view of runaway stars with the solar system at the origin. The positive X direction is to Galactic Center.

Figure 7 illustrates how the stars in Kobulnicky et al. (2019b) are distributed above and below the Sun. In Figure 7 we can see how this compares to the galaxy as a whole.

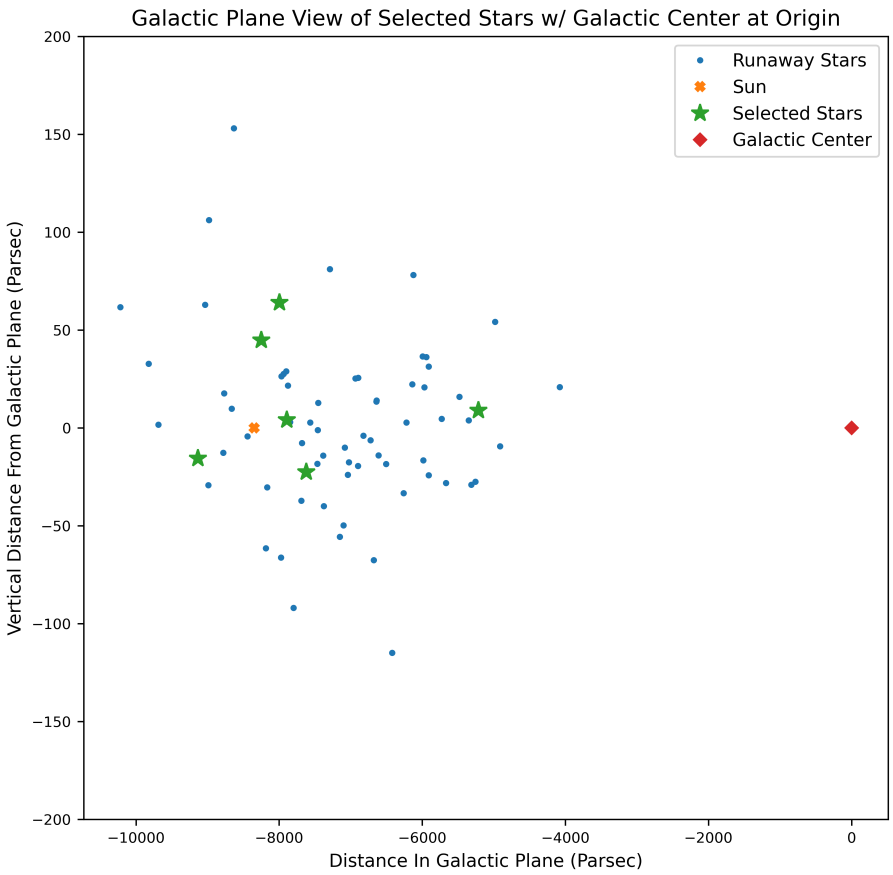

Figure 7. Galactic Plane view of runway stars with Galactic center at the origin.

Figure 5 presents a similar shift of stars to illustrate their positions relative to the center of the MW. Combined with Fig 5 we are able to verify that the selected group of

stars are distributed in the galactic plane around the sun. The distribution of runaway stars with verifiable bow shocks should be sufficient to constrain how the ISM composition varies around the Sun and Galaxy as a whole.

2.7. *WISE Images of Selected Stars*

For this paper we are focusing on the specific set of runaway stars in Table 1. To verify that the selected star is a good candidate to simulate, we inspected the infrared image of the progenitor star and resulting bow shock in the WISE database[4]. Each star was observed in the four WISE bands, which correspond to wavelengths of 3.4, 4.6, 12, and 22 μm respectively.

We started by looking at each bow shocks in the four WISE bands separately. Each shock was clearly defined in the 4.6, 12, and 22 μm bands, while some of the selected stars had no shock visible in the 3.4 μm band. We then used the multicolor tool to view an RGB composite of three WISE band images with the red, green and blue colors corresponding to a specific WISE band. For the stars where the shock was visible in all four WISE bands we set the 3.4 μm band as red, the 4.6 μm band as green, and the 12 μm band as blue. In the composite images of the stars where the 3.4 μm band is not clearly visble we instead set the 4.6 μm band as red, the 12 μm band as green, and the 22 μm band as blue to highlight the shock.

By looking at the composite imaged, we confirmed that each star has a visible bow shock in the infrared, that is clearly separated with respect to the progenitor star. This verified that a distinct bow shock was present for each selected stars. We created an

[4] https://irsa.ipac.caltech.edu/applications/wise/

RGB image from the downloaded composite images of each star, which we provide in Figure 8, along with two distance scales for each star: arc minutes and parsecs. This image illustrates that the geometry of each bow shock differs due to the omnidirectional nature of v_*.

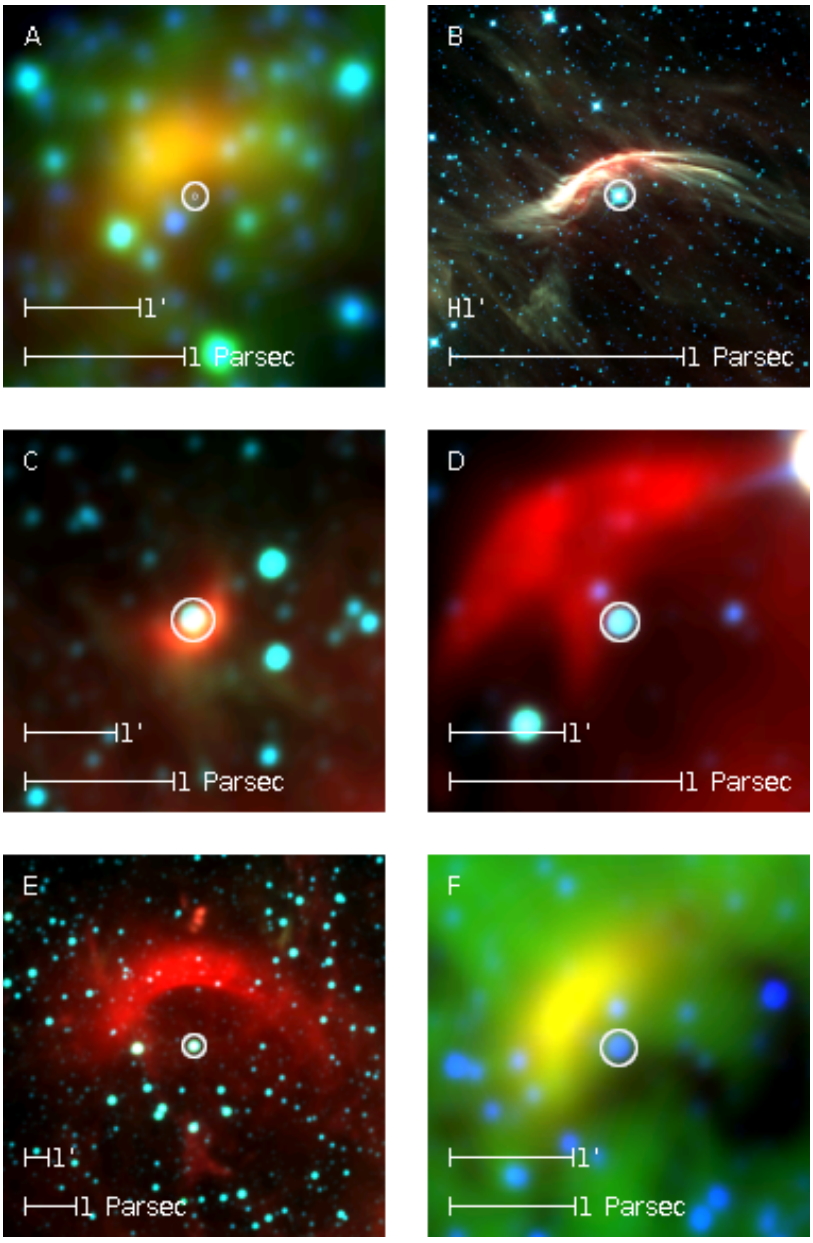

Figure 8. WISE images of selected runaway stars. Each star and the WISE bands in RGB order are as follows: A. G000.1169-00.5703 in bands 4,3,2, B. ζ Ophiuchi in bands 3,2,1, C. KGK 2010-10 in bands 3,2,1, D. CPR 2002A37 in bands 3,2,1, E. BD+43 3654 in bands 3,2,1, F. G342.5873+00.1600 in bands 4,3,2. The top scale given is distance in arc minutes and the bottom scale is distance in parsecs.

In Figure 8, each star is at the center of the image. The different R(0) for each star are identifiable in Figure 8 and match the numerical values given in Table 2. Also visible is the variation in both shape and size for each bow shock. This is to be expected given the different $\dot{M}$, v_* and direction of travel for each star.

We note a few unique structures in the bow shocks. For ζ Ophiuchi and CPR 2002A37, the shock is asymmetrical. As highlighted in Meyer et al. (2021), this structure may be due to v_{*r} and the angle of v_* with respect to v_{ISM} around the star. This difference in direction causes a sheer effect, producing the asymmetrical shock seen (van Buren et al. 1995). This is in contrast to the shocks for the other stars where we see a relatively symmetrical shock. Additionally, we see that the shock of KGK 2010-10 is located relatively close its progenitor star. This is to be expected since each star is not necessarily traveling perpendicularly to our line of sight. This implies that for some stars, the uncertainty in R(0) can be quite high.

Resolution diminishes with distance. The shock of BD+43 3654 is particularly interesting because it is still quite well defined even though G342.873+00.1600 is the only star in our sample set that is further away. We also are able to see that the bow shock of BD+43 3654 is almost three times larger than the bow shock of CPR 2002A37, which is the closest star in mass to BD +43 3654. The size of BD +43 3654's shock, despite its distance from us, makes it a particularly interesting star in the survey. For this reason we included BD +43 3654 in the simulations even though it is no longer a main sequence star.

3. SIMULATIONS

3.1. *Star Parameters*

We take the parameters for M_*, R_*, v_*, T_*, L_*, $\dot{M}$, and ρ_{ISM}) necessary for the simulations from the VizieR database of Kobulnicky et al. (2019b)[5] and the work of Green et al. (2022). The parameters for L_{Edd}, Γ, β_w, v_w, R_0, T_{ISM}, and t_{cross} are derived using the methodology of Meyer et al. (2014), and Eldridge et al. (2006). We use the notation R_0 to differentiate between the measured $R(0)$ and value calculated using Equation 9. ζ Ophiuchi's v_* has recently been calculated by Green et al. (2022) to be higher than the value given by Kobulnicky et al. (2019b). Therefore for ζ Ophiuchi we use the more recent v_* of 38 $km\,s^{-1}$ which corresponds to previous calculations by Mohamed et al. (2012).These required physical values can be found below in Tables 2 and 3.

[5] https://vizier.cds.unistra.fr/viz-bin/VizieR?-source=J/AJ/158/73

Table 2. Runaway Star Known Parameters

Name	M_*	v_*	R_*	T_*	L_*	$\dot{M}_{low}$
	$M_\odot$	$km\,s^{-1}$	$R_\odot$	(K)	$10^4\ L_\odot$	$10^{-10}\ \frac{M_\odot}{yr}$
G000.1169-00.5703	26.0	16.3	9.4	35500	12.000	2639
ζ Ophiuchi	19.0	38.0	7.2	31000	4.2	117
KGK 2010-10	22.0	41.6	8.5	33400	7.9	474
CPR 2002A37	37.0	78.1	11.1	41500	32.0	121619
BD+43 3654	58.0	37.7	19.0	40700	87.0	197923
G342.5873+00.1600	32.0	16.7	10.2	38100	19.0	2244

NOTE—From Kobulnicky et al. (2019b) and Green et al. (2022). $\dot{M}_{low}$ is minimum $\dot{M}$ with error.

Using Equations 9, 11 and 13, we calculated R_0, v_w and t_{cross} for each star.

Table 3. Runaway Stars Calculated Parameters

Name	β_w	L_{Edd}	Γ_w	v_w	R_0	t_{cross}
		$10^4\ L_\odot$		$km\,s^{-1}$	Pc	Myr
G000.1169-00.5703	2.6	84.0	0.14	1535.61	0.261	$2.1x10^{-2}$
ζ Ophiuchi	2.6	61.4	0.07	1562.3	0.052	$1.5x10^{-2}$
KGK 2010-10	2.6	71.1	0.11	1512.1	0.085	$2.7x10^{-3}$
CPR 2002A37	2.6	119.5	0.26	1561.1	0.408	$7.8x10^{-3}$
BD+43 3654	2.6	187.4	0.46	1283.8	0.955	$4.2x10^{-2}$
G342.5873+00.1600	2.6	103.4	0.18	1596.8	0.266	$3.1x10^{-2}$

NOTE— Processed Data from Kobulnicky et al. (2019b)

3.1.1. *Cooling and Heating*

Each simulation includes the relevant heating and cooling physics present in the bow shock. To implement this, we need to calculate the required heating and cooling curves over a large range of temperatures. Calculations for the cooling and heating tables were performed using the method outlined in Meyer et al. (2014). The cooling and heating curves for Λ_{Cool} and Γ_{Heat} are created separately before being combined using Equation 6. The cooling curve, Λ_{Cool}, is comprised of different cooling effects that are calculated independently then combined using Equation 16 from Meyer et al. (2014):

$$\Lambda_{Cool} = \Lambda_{H+He} + \Lambda_Z + \Lambda_{RR} + \Lambda_{FL} \tag{16}$$

Here the cooling components Λ_{H+He}, Λ_Z, Λ_{RR}, and Λ_{FL} are the hydrogen plus helium, metals, recombination rate, and forbidden line cooling respectively. To realistically model the cooling curves for these effects, a large range of temperatures is required with a large number of distinct temperature values. However, none of the data sources for the various Λ_{Cool} functions match these criteria. Therefore, it is necessary to interpolate more data points from the given data.

For our Λ_Z cooling curve we obtained the metal cooling table from Wiersma et al. (2009), who gives cooling values for various redshifts, and n_H. To model the metal cooling we selected the $n_H = 1$ table for zero redshift. As each star has a different velocity, and ρ_{ISM}, this allows our simulation to be consistent between stars. We present the resulting interpolated cooling curve below for temperatures greater than $10000K$.

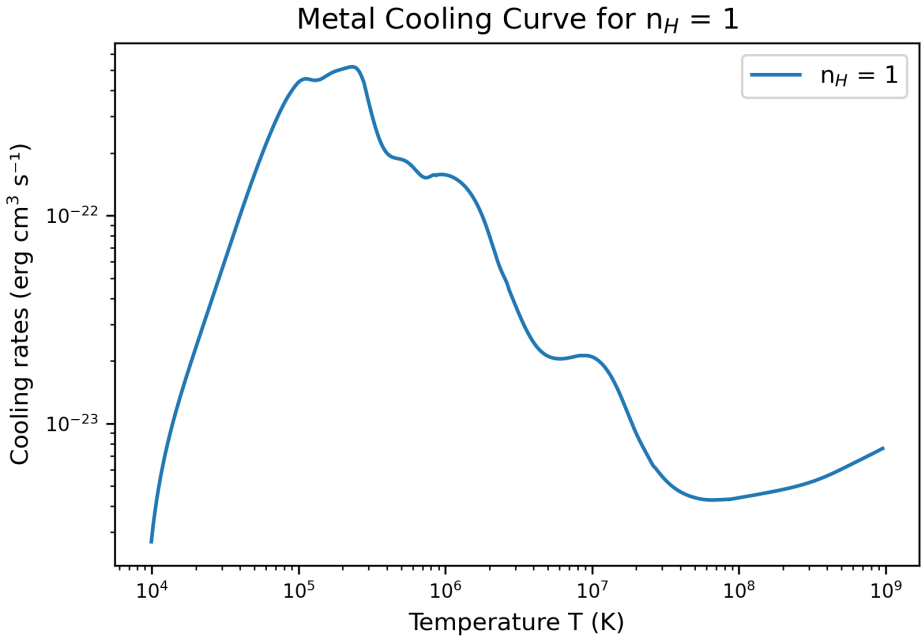

Figure 9. Cooling curve for Λ_Z. Data is interpolated from Wiersma et al. (2009). Below $10^4 K$ the cooling effect becomes negligible.

In Figure 9, Λ_Z is strongest between 10^4 and 10^7 Kelvin. Because of the low number of temperature values in the data, we want to expand the data set from 353 temperature to 2079. Because there is no single function that represents an entire Λ_Z, or Λ_{H+He} cooling curve (Wiersma et al. 2009), a series of 6^{th} order polynomials were required to interpolate the data into a set of functions that when combined represents the entire curve. This allowed us to expand the cooling tables range from $10^2 - 10^9 K$ to $10^{-1} - 10^9 K$. This range matches the temperature range of Meyer et al. (2014). Simultaneously we were able to increase the number of unique temperatures from 353 to 2079.This increase in resolution allows for more precise heating and cooling effects on each cell every time-step.

To obtain the Λ_{H+He} curve, we started with solar cooling curve in Figure 10 from Wiersma et al. (2009) below.

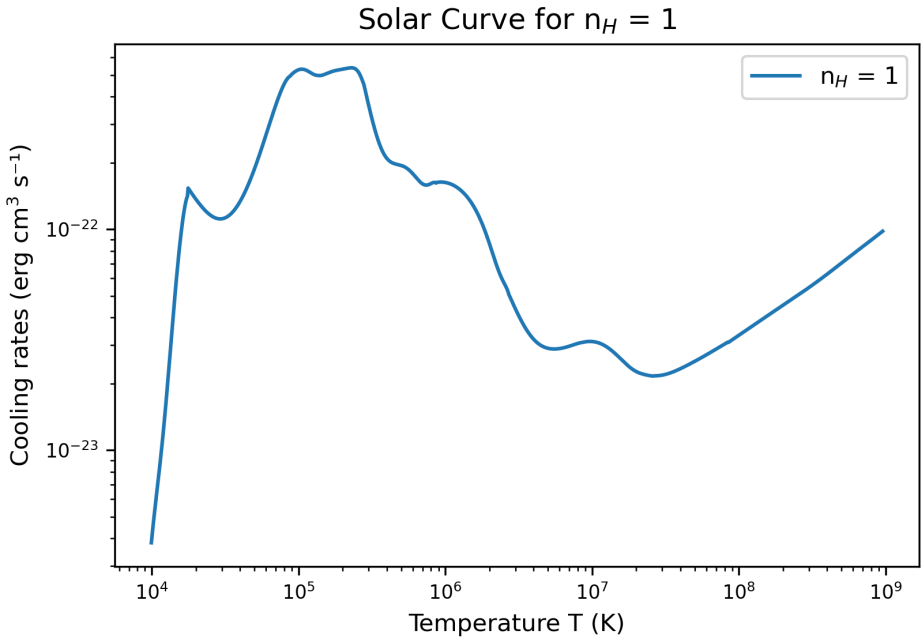

Figure 10. Solar cooling curve. Data is interpolated from Wiersma et al. (2009). Below $10^4 K$ the cooling effect becomes negligible.

In Figure 10, the combined cooling effects of the Λ_{H+He} and Λ_Z cooling curves is presented as (Λ_{Solar}). The same polynomial interpolation technique used for Λ_Z was then applied to increase the data range and resolution. By subtracting Λ_Z from Λ_{Solar} we obtain the cooling curve for Λ_{H+He} seen below in Figure 11 for temperatures greater than $10000K$.

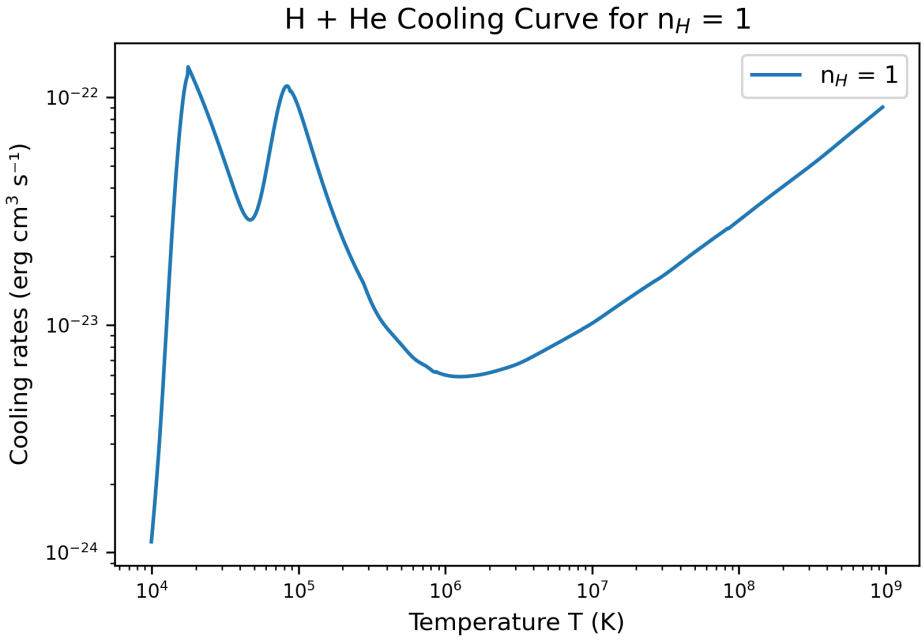

Figure 11. Cooling curve for Λ_{H+He} with zero redshift and $n_H = 1$. Data is interpolated from Wiersma et al. (2009). Below $10^4 K$ the cooling effect becomes negligible.

Here, Λ_{H+He} is strongest between 10^4 and $10^6 K$ with an increase in strength after $10^6 K$.

The Λ_{RR} cooling function was created assuming the case B energy loss (β_B). This comes from assuming that the absorption profile from level 1 to n for an atom are balanced by the inverse spontaneous transitions Baker & Menzel (1938). To determine β_B, we assume the $T_e^{1/2}(\beta_B)$ from Table 1 of Hummer (1994) and divided the value by the $T_e^{1/2}$ to get the recombination rate in $erg\,cm^3\,s^{-1}$. Next we utilized a power series interpolation with $R^2 > 0.99$ to expand the resolution of the data set. The final cooling curve is then calculated for $T < 60000 K$ using the same temperature scale as Λ_Z.

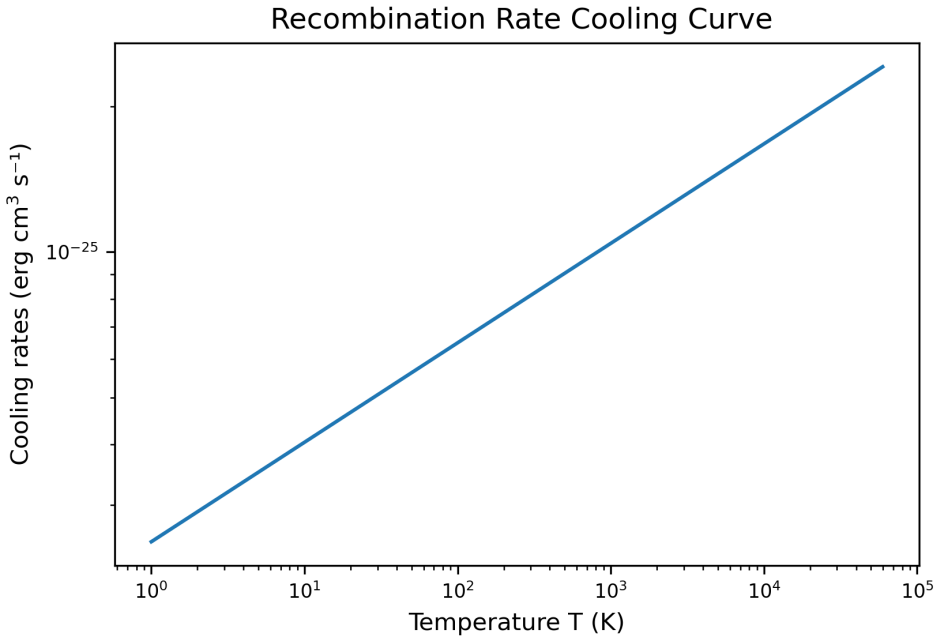

Figure 12. Λ_{RR} cooling curve.

The forbidden line cooling curve we obtain by using equation A9 from Henney et al. (2009) below.

$$\Lambda_{FL} = 2.905x10^{-19} z_O n_e n_p e^{\frac{-T_1}{T} - \left(\frac{-T_2}{T}\right)^2} \; erg\, cm^3\, s^{-1} \tag{17}$$

In Equation 17, z_O is the oxygen abundance, while $T_1 = 33610K$ and $T_2 = 2180K$, respectively (Henney et al. 2009). For the simulations we assume a solar oxygen abundance of $n_0/n_H = 4.89x10^{-4}$ (Asplund et al. 2009), identical to Meyer et al. (2014). Because of low cooling rates and discontinuities at low temperatures ($T < 8000K$), we only incorporated Λ_{FL} from $8000K$ to $60000K$.

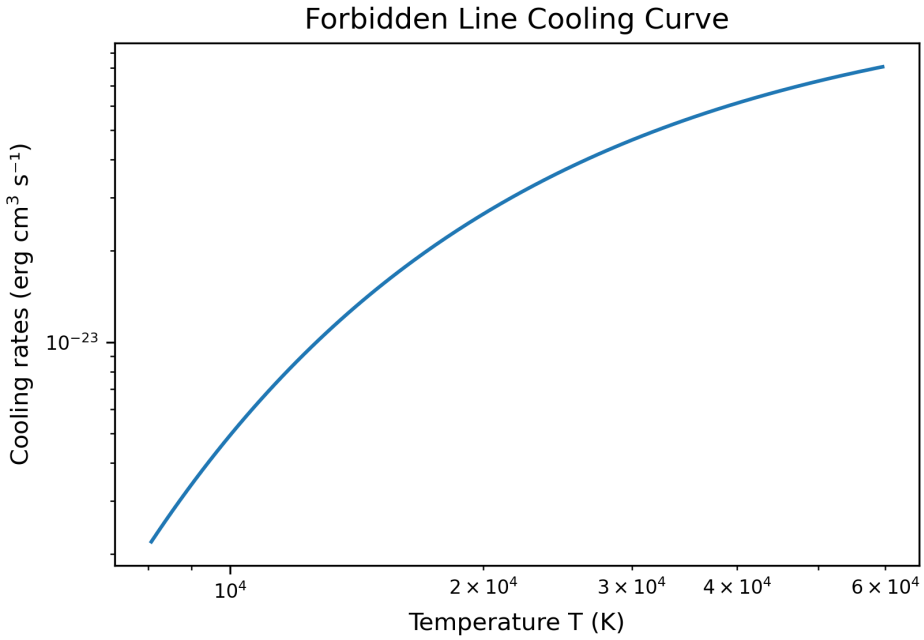

Figure 13. Λ_{FL} cooling curve.

The heating function (Γ_{Heat}) in Equation 6 is Equation 6.9 from Spitzer (1978) below.

$$\Gamma_{Heat} = \frac{2.07x10^{-11} n_e n_p}{T^{1/2}} \left\{ \overline{E}_2 \phi_1(\beta) - kT_{\chi_1}(\beta) \right\} \tag{18}$$

Where n_e, and n_p are the number of electrons and protons respectively which is calculated separately for each star. $\overline{E}_2$ is the kinetic energy of newly created photoelectrons derived from interpolating the data from Spitzer (1978) table 6.1 at various temperatures T, $\phi_1(\beta)$ is the combination coefficient derived from interpolating the data from Spitzer (1978) table 5.2 at various temperatures T, k is Boltzmann's constant, and $T_{\chi_1}(\beta)$ is the energy gain function derived from interpolating the data from Spitzer (1978) table 6.2. Unlike the cooling curves, the heating curve will be different for each star, because of the dependence on R_s, and n_h. This method allows us

to separately calculate the heating curve in the vicinity of each star. Finally, we combine the heating and cooling curves using Equation 6.

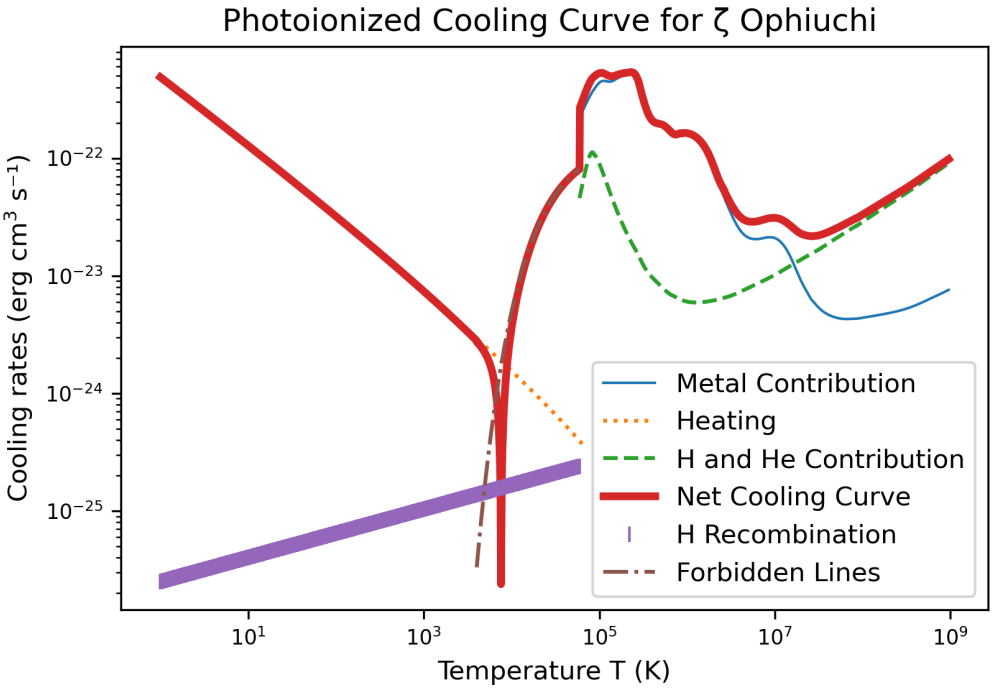

Figure 14. Combined Photo-ionization cooling curves of ζ Ophiuchi.

In Figure 14, we present the cooling and heating curves representative of the environment around ζ Ophiuchi, along with the combined heating and cooling curve in red. The only difference between the cooling curves for each star id Γ_{Heat}, so the combined curve of ζ Ophiuchi is similar to the ones for the other five stars. Around $8000\,K$ we see the minimum value of the combined curve which will be used to set T_{ISM} for each simulation. Briefly we discuss the curve in Figure 14. At $T \sim 0-8000K$ the curve is dominated by the heating effects of the star. From $T \sim 8000-60000K$, Λ_{FL}

is dominant. At temperatures between $T \sim 60000 - 10^{6.5} K$ the cooling is dominated by the metal cooling. Above $T \sim 10^{6.5} K$, the curve is dominated by unbound (x-ray, scattering, free-free) emission from the gas.

3.2. *PLUTO Code*

To run our simulations, we need to solve the hydrodynamic equations need to be solved for each time step. We accomplished this using the PLUTO code by Mignone et al. (2007) which is based on the work of Godunov & Bohachevsky (1959). PLUTO is a readily available, open source numerical hydrodynamics simulation code designed for astrophysics simulations in the C programming language. It allows us to iteratively solve the hydrodynamic equations for a given set of input parameters. The code is designed to solve a system of conservation laws of the form (Mignone et al. 2007).

$$\frac{\partial \mathbf{U}}{\partial t} = -\nabla \cdot \mathbf{T}(\mathbf{U}) + \mathbf{S}(\mathbf{U}) \tag{19}$$

Where $\mathbf{U}$ is a state vector of conserved quantities, $\mathbf{T}(\mathbf{U})$ is a 2nd rank tensor whose rows are the flux components of $\mathbf{U}$ and $\mathbf{S}(\mathbf{U})$ is the source terms (Mignone et al. 2007). While components of $\mathbf{U}$ are the primary variables being updated, the fluxes are computed using a different set of physical quantities of the vector form $\mathbf{V}$. The conservation laws in Equation 19 are numerically integrated using finite volume shock-capturing schemes. This integration is done in three steps and establishes the framework of the PLUTO code (Mignone et al. 2007). The PLUTO code also supports Message Passing Interface, or MPI, which allows for parallel processing of simulations.

PLUTO has three main parameter files that can be easily modified to set up a simulation. When setting up the code, these files are generated as *definitions.h*, *pluto.ini*, and *init.c* (Mignone et al. 2007). The setup of a new simulation is done in a python scripted user interface (UI), which allows for the selection of the basic and physics dependent parameters for the simulation. Simultaneously, the UI allows for defining the independent variables of the simulation, and to run the code in parallel.

The *definitions.h* file is auto generated based on the setup parameters chosen by the user. These are divided into two main areas: Basic, and Physics-Dependent options. In the basic options we are able to select the core parameters of our simulations: Physics, Dimensions, Geometry, Body Force, Cooling, Reconstruction, Time Stepping, Tracers, Partials, and User Defined parameters. The physics dependent options for Hydrodynamic simulations include: End of State, Entropy Switch, Rotating Frame, Thermal Conduction, and Viscosity. We can also change the system constants for unit measurements: length, velocity, and density. Other predefined macros can also be implemented in the *definitions.h* file. Once these files are set up by the user, a make script is used to set up the PLUTO code.

The *pluto.ini* file is used to assign numerical values to simulation parameters, select our desired solver, declare the boundary conditions for each axis, and the grid geometry (Mignone et al. 2007). This file is also the easiest to modify while setting up simulations, as it allows us to quickly change the values of various simulation parameters without needing to run a make script to update the rest of the code. The $Pluto.ini$ file also allows us to control both when and how often run data are saved during a simulation.

In *init.c*, we are able to set up initial conditions, user-defined boundary parameters, a separate analysis code (optional), and the desired body forces (optional) (Mignone et al. 2007). The initial conditions are applied over the entire area of the simulations. Inside of the user defined boundary section we can setup both interior boundaries along with edge conditions as needed. The user defines specific values in the initial volume and boundary conditions: density, velocity, and pressure. These values can either be imported from the user defined variables in $pluto.ini$, or calculated at each time step with user specified equations (Mignone et al. 2007).

3.3. *PLUTO Code Setup*

We then set up the PLUTO v4.4 hydrodynamics code by Mignone et al. (2007) to solve the system of hydrodynamic equation over each time step. Each simulation is set up based on the method outlined by Meyer et al. (2014). The simulations use a parabolic reconstruction, which uses the piecewise parabolic method of Mignone (2014) to reconstruct the data between time steps. In the piecewise parabolic method, the parabolic interpolant is found using the cell average and extrapolated values of the left and right edges. Time stepping is handled using a 3rd order Runge-Kutta total variation diminishing scheme. The flux at each time step is then found using a Harten, Lax, Van Leer (HLL) approximate Riemann Solver. The HLL solver uses the collision-less Boltzmann equation to find the approximate Riemann solution for each time step, see (Harten et al. 1983). which guarantees that the pressure will be positive when computing the flux at the edges of a cell, and if the pressure is negative, the simulations automatically stop (Mignone et al. 2007).

Modifying the *init.c* file allows us to input starting parameters for ρ_{ISM}, ρ_w, v_*, v_w, and p (calculated using equations 5 and 10). In the initial conditions we set up a background area with the ambient density for the star from Kobulnicky et al. (2019b) and found the pressure using Equation 5 for T_{ISM} at equilibrium in the cooling curve. We set the gas to move in the y-axis at v_*. Instead of defining an equal sized grid around the origin, we set our domain to include y-axis and the positive x-axis. This change does not affect the results of our simulations but allows us to save considerable computation time. Inside of the grid we initialize the star with its stellar wind centered at the origin $(0,0)$. Our wind parameters are from finding ρ_w in a circle with a radius of 20 cells from the origin. This is identical to Meyer et al. (2014).

Our simulations assume a 2D cylindrical coordinate system, where the $z-axis$ of the 3D cylindrical coordinate system is set to a single value, giving us a polar coordinate system (Mignone et al. 2007). At $x = x_{max}$, and $y = y_{min}$ borders we utilized outflow boundary conditions. We set the ISM material to flow inwards with velocity v_* at the $y = y_{max}$ boundary. The stellar wind is generated in a circle 20 pixels in radius, with the center at the origin, by finding $\rho_w = 0.1pc$ and then scaling it to the distance r from the center. The $x = x_{min}$ border is set to a reflective boundary condition, which allows us to restrict our simulations to positive x values by replicating the interactions between the $x-negative$ and $x-positive$ gas at the boundary.

3.4. *Simulation Setup*

To start a simulation, we first set up the *pluto.ini* file with the initial parameters: $R(0)$, n_{ISM}, v_*, v_{wind}, T_{ISM} and $\dot{M}$ from Kobulnicky et al. (2019b) and Green et al. (2022). We calculate the faintest possible bow shock by assuming $\dot{M}$ is at the low end of the

associated 3σ error given by Kobulnicky et al. (2019b). This allows us to account for any errors in the data given when running our simulations.

Our first time step is set to be 0.1 years. The grid boundaries were set to $y_{max} \approx R(0) * 4$ for the positive and negative y-axis and $x_{max} = y_{max}$ or $x_{max} = 2 * y_{max}$ for the x-axis depending on the bow shocks width. Each axis minimum resolution is set 400 in the y-axis and either 200 or 400 in the x-axis depending on the stability of the shock at the $x - axis$ boundary. A simulation then runs until it reaches a preset time, (T_{stop}), which is set to $\sim 60 * t_{cross}$. After initial setup we ran the simulation for $10^5 - 10^6$ time steps to verify that the resulting bow shock is stable.

Some initial simulations resulted in an unstable bow shock where $R(0)$ expands continuously instead of reaching a stable limit. Because the stability of the shock depends on the ram pressure of the stellar wind and ISM to be balanced, if $R(0)$ continued to expand past the theoretical limit (see Equation 14) we needed to adjust our simulation setup to bring the parameters back into balance. To verify that the simulated shock was an accurate representation of the star we looked at the shock over the first 100000 time-steps to verify that the $R(0)$ simulated matched the data.

If the simulation was not a match to the data, we adjusted each simulation using the following methodology. If the winds termination zone was too far from $R(0)$, we started by changing the resolution to bring it closer to $R(0)$. If this did not work without lowering the resolution below $200X400$ pixels, we then adjusted the grid size to be between $\sim 3 - 10\, R(0)$ to account for rounding in the grid size calculations and different $R(0)$. Our final simulation parameters for each star can be seen below in Tables 4 and 5.

Table 4. Simulation Physical Parameters

Star Name	R(0)	n_{ISM}	T_{ISM}	v_*	v_{wind}	$\dot{M}$	t_{cross}
	Pc	cm^{-3}	K	kms^{-1}	kms^{-1}	$(10^{-10}\ \frac{M_\odot}{yr}\ )$	Myr
G000.1169-00.5703	0.261	41	7748.8	16.3	1535.6	1530	$1.6x10^{-2}$
ζ Ophiuchi	0.052	9	7596.2	38.0	1562.3	72	$1.4x10^{-2}$
KGK 2010-10	0.085	11	7672.1	41.6	1512.09	289	$2.7x10^{-3}$
CPR 2002A37	0.408	35	7983.6	78.1	1561.1	72391	$5.0x10^{-3}$
BD+43 3654	0.955	29	7983.6	37.7	1283.8	125117	$2.4x10^{-2}$
G342.5873+00.1600	0.266	20	7904.6	16.7	1596.8	786	$1.6x10^{-2}$

NOTE—Physical parameters for each simulation. Each star is listed with the relevent parameters imputed into the pluto.ini file.

Table 5. Simulation Spatial Parameters

Star Name	x_{max}	y_{max}	N_x	N_y	t_{stop}
	Pc	Pc			Myr
G000.1169-00.5703	5.0	2.5	400	400	1.3
ζ Ophiuchi	0.86	1.72	400	400	0.1
KGK 2010-10	1.0	1.0	200	400	0.2
CPR 2002A37	4.0	4.0	200	400	0.5
BD+43 3654	12	12	200	400	2.0
G342.5873+00.1600	6.3	3.15	400	400	1.2

NOTE—Spatial parameters for each simulation. Each star is listed with the relevent parameters imputed into the *pluto.ini* file.

Tables 4 and 5 gives an overview of the simulation parameters that we imputed into the *pluto.ini* file before each run. The y_{min} value is the same as the one used for y_{max} in the negative direction. Each run takes approximately 1-3 days to complete when run in parallel over 3 CPU cores. These parameters are representative of the actual runaway stars as they assume that v_* is in the same direction as v_{ISM}. While this will not have much effect on the simulations for stars with a v_* that is perpendicular to our line of sight, stars with a v_* that includes significant motion towards or away from the sun will be less accurate.

4. ANALYSIS

4.1. *Simulation Results*

After running each simulation, we first created a composite plot of the density for each simulation.

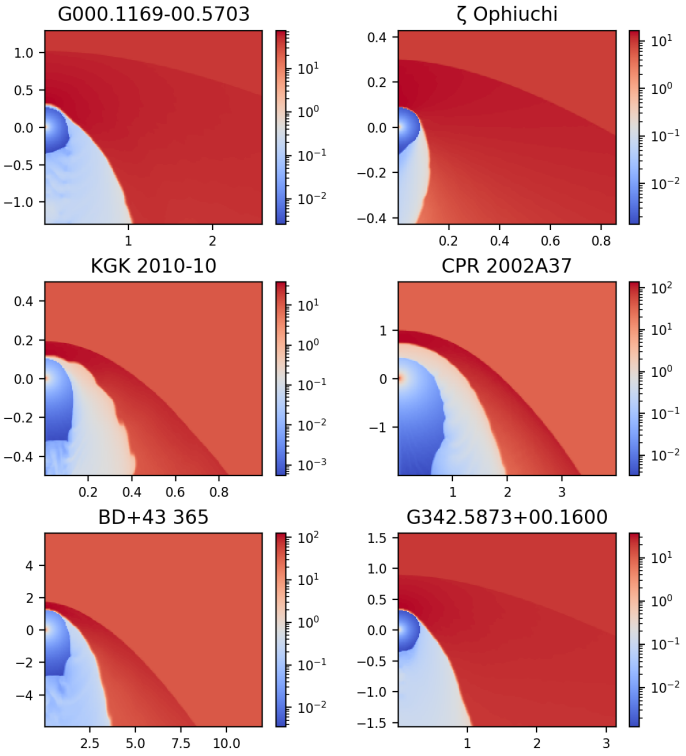

Figure 15. Plot of $\log \rho_{gas}$ for each bow shock. The X and Y axis are scaled in parsecs, and the color bar is in the log scale for density of particles. The plots are truncated from the full result grid to highlight the bow shock. Each plot has units of $\log cm^{-3}$.

In Figure 15 we can see the a log-scaled density plot of each star and its bow shock. The shock for ζ Ophiuchi, G000.1169-00.5703, and G342.5873+00.1600 are thicker than the other stars. We found that the bow shock of ζ Ophiuchi was the hardest to accurately simulate. We believe this is caused by the highly asymmetrical shock seen in the WISE image (see Figure 8), making accurate measurements of its $R(0)$ from these images as done in Kobulnicky et al. (2019b). Even though ζ Ophiuchi has a hard to reproduce shock, we included it in our simulations due to its close proximity. While wider than the rest of the shocks, we still can see that they are well-defined with the highest density at the front of the shock. CPR 2002A37 has the largest region of shocked stellar wind in the direction of travel. Because we are looking for an average of the emission in the highest density zone of each shock with the lowest possible $\dot{M}$, these small variations will have a negligible result on our emission calculations.

4.2. *Comparison to Meyer et al. (2014)*

Looking at Figure 15, we can see that each bow shock has a different structure based on the input parameters. Because each simulation is run using the same $init.c$ file, a single star can be compared to the previous work by Meyer et al. (2014) as a representative of the the whole set of simulations. We chose to compare the simulated shock of KGK 2010-10 with the results of Meyer et al. (2014) MS2040 star. KGK 2010-10 was selected because of the similarities between its M_* and v_* and the MS2040 run by Meyer et al. (2014). This allows us to verify that our simulations for each star are accurately set up. Below we can see the results of KGK 2010-10's simulation and the MS 2040 star from Meyer et al. (2014).

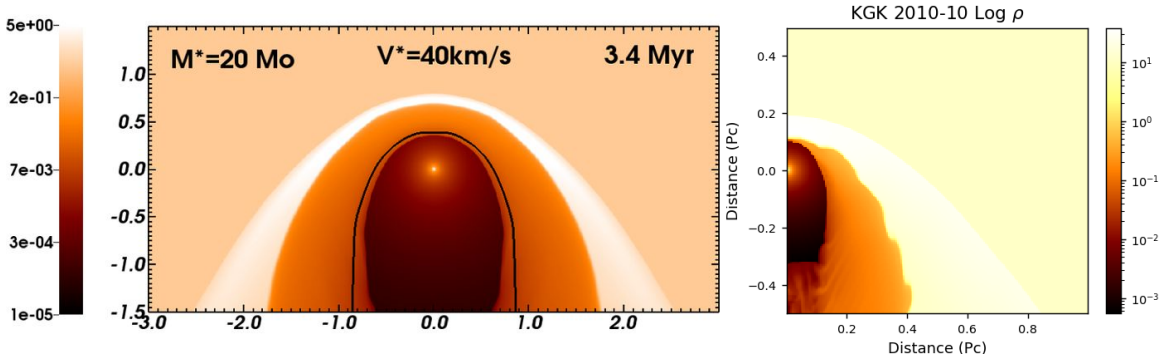

Figure 16. Comparison between the MS2040 (left) star of Meyer et al. (2014) and KGK 2010-10 (right). The X and Y axis are in parsecs.

In Figure 16, we see that the overall shape of the bow shocks and the distribution of gas is the same. The standoff distance between the stellar wind and the brightest part of the bow shock is much shorter for the KGK 2010-10 simulation. This is a result of setting the termination distance for the stellar wind much closer to R(0) than in Meyer et al. (2014). The ISM for KGK 2010-10 is also much denser than the ISM for the MS2040 star, which accounts for the different size of each shock.

4.3. *Comparison to WISE*

We also want to verify that the simulations are accurately reproducing observed bow shocks. For this comparison we selected the simulation results representative of BD +43 3654 to compare with the composite image from the WISE database. BD +43 3654 was selected because the observed shock is highly symmetrical and well defined from its progenitor star, which is similar to how our simulations are set up allowing for comparisons between the star and its simulation.

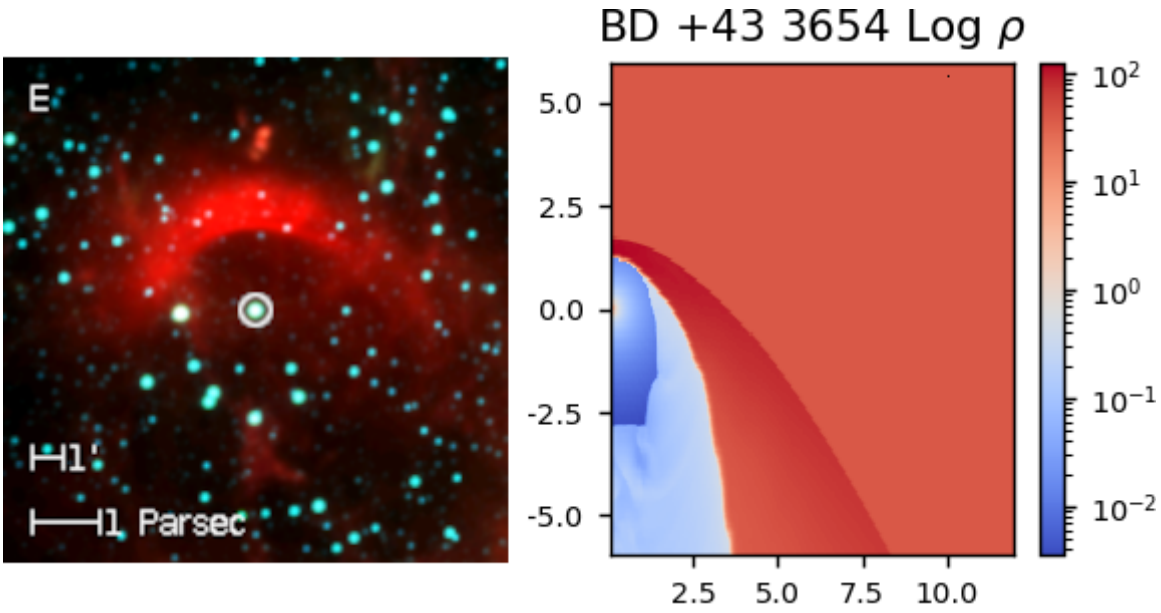

Figure 17. Image of BD +43 3654 from WISE (left) and simulations (right). The distance is in parsecs, and the bar represents log density

Looking at Figure 17, we can infer that the overall shape of the simulated bow shock is similar to WISE observations. The brightest part of BD +43 3654's shock is in the direction of travel In our simulation, the densest part of the shock is in front of the star, which is what we would expect from the WISE image. Each simulated shock has a lower thickness than the actual image, which is understandable due to the simulation using the lowest value of $M_{\odot}$ with error taken into account.

4.4. *Mean Output of Emitting Region*

We analyzed the results of each simulation to find the bow shock luminosity (L_{Bow}) for the $H\alpha$, $HeI\,\lambda$5876Å and $[OIII]$ lines. To measure L_{Bow}, we corrected for the stellar wind and un-shocked ISM present in the simulation results (Mohamed et al. 2012). The stellar wind was corrected for by finding the regions where $\rho < \rho_{ISM}$ and then setting

ρ_{ISM}, $p_{ISM}$and T_{ISM} to zero. We removed the un-shocked ISM by finding the value for ρ_{ISM} and T_{ISM} in each cell, and set ρ_{ISM}, $p_{ISM}$and T_{ISM} to zero if either property was than their initial value. We illustrate the results of this process with the density plot of KGK 2010-10 in Figure 18.

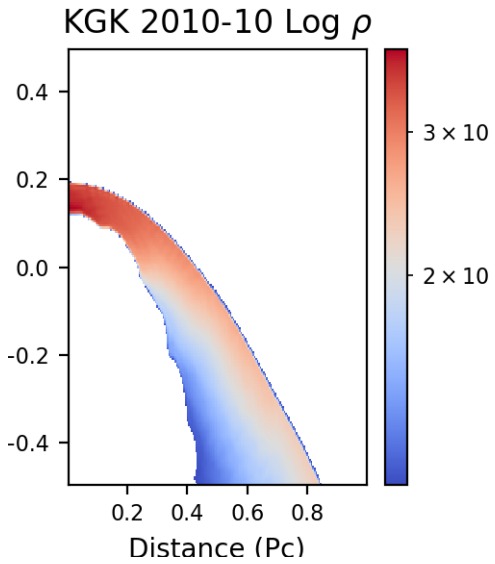

Figure 18. Log ρ plot of KGK 2010-10 simulation with non shock regions set to zero. The axis are in parsecs, and the scale is in $log(\rho)$. The plot has units of log cm^{-3}.

In Figure 18, the bow shock with the non-shock region parameters set to zero. This leaves us with only the bow shock of the star. The blue band at the front represents residual high temperature and low-density shocked ISM material. From Figure 8 we see that the brightest part of a shock is in the direction of travel. In Figure 18 we see that the densest part of the shock is in the front. Since the brightest part of a runway stars bow shock is also in the direction of motion, we can ignore the shocked material behind the star in our luminosity calculations. To account for this we set ρ, p and T to zero for

each cell where $y < 0$. This gives us our final region for calculating the luminosity of each bow shock.

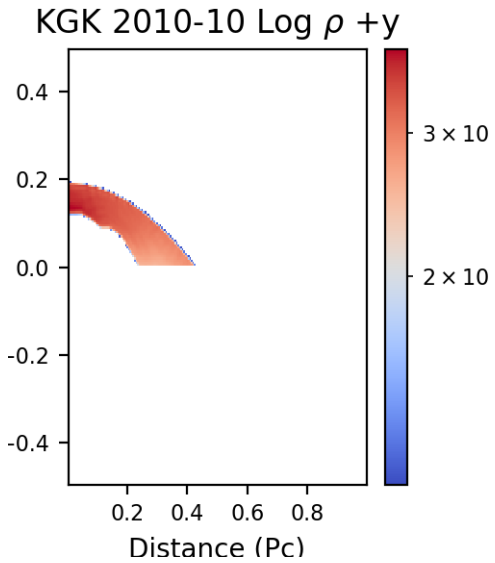

Figure 19. Final region for luminosity calculations. The axis are in parsecs, and the scale is in $log(\rho)$. The plot has units of $\log cm^{-3}$.

The final region for KGK 2010-10 luminosity calculations can be seen in Figure 19. Here we can see that by setting the parameters of the $y < 0$ regions to zero, we are able to highlight the densest part of the shock. This gives us our ideal region for calculating the mean emission in $H\alpha$, $HeI\,\lambda 5876$Å and $[OIII]$ lines. After the un-shocked material was removed, we calculated the luminosity for a given (Λ) cooling curve using equation 20 below (Meyer et al. 2014).

$$L_{shock} = 2\pi \iint_D \Lambda(T) n_H^2 R dR dz \tag{20}$$

Here, D is the surface area of integration, $\Lambda(T)$ is the cooling rate calculated at a point (x,y) from Equation 5 and n_H is the number density at the same point. To determine $L_{H\alpha}$ we used equation A1 from Meyer et al. (2014) which is derived from an interpolation of Table 4.4 in Osterbrock (1989).

$$\Lambda_{H_\alpha} = 1.21x10^{-22} T^{-0.9} n_e n_p \;\; erg\, s^{-1}\, cm^{-3} \tag{21}$$

Using the same interpolation method with table 4.6 of Osterbrock (1989), we are able to get Equation 22 for $HeI\,\lambda$5876Å below.

$$\Lambda_{He\lambda 5876\text{Å}} = 4.27x10^{-23} T^{-1.1} n_e n_p \;\; erg\, s^{-1}\, cm^{-3} \tag{22}$$

The luminosity of the $[OIII]$ emissions is calculated using Equation 17, which is restated below as Equation 23. Again T1 = 33610K and T2 = 2180K Henney et al. (2009).

$$\Lambda_{[OIII]} = 2.905x10^{-19} z_O n_e n_p e^{\frac{-T_1}{T} - \left(\frac{-T_2}{T}\right)^2} \;\; erg\, cm^3\, s^{-1} \tag{23}$$

In Equations 21 - 23 n_e and n_p are the number density of electrons and protons at a given point in the emitting region. We calculated the values of n_{e_i} and n_{p_i} for the $\Lambda_{H\alpha}$, Λ_{OIII}, and $\Lambda_{He\lambda 5876\text{Å}}$ emission lines where i = 1, 2, and 6 for H, He and O respectively.

$$n_{p_i} = \frac{m_h A_n}{u w_i} cm^{-3} \tag{24}$$

Here, m_H is the mass of a hydrogen atom, A_n is the atomic mass of the element, u is an atomic mass unit, and w_i is the mass fraction of the element derived from the

metallically. We then use the results of Equation 24 in Equation 25 to get the number of electrons.

$$n_{e_i} = n_{p_H}(1.0 + 0.5A_z(1.0 - w_H - w_{He}))\ \ cm^{-3} \tag{25}$$

Where n_{p_H} is the number of hydrogen atoms from Equation 24, A_z, which we assume to be 30.0, is the mean atomic weight of heavy elements, w_H and w_{He} are the hydrogen and helium mass fraction, respectively. We used Equations 21 - 25 to find the emission at each grid particle of the simulation. Taking the average of the emission in the $y > 0$ region averaged over the volume, we measured the average cooling rates of the $\Lambda_{H\alpha}$, Λ_{OIII}, and $\Lambda_{He\lambda 5876\text{Å}}$ lines for the bow shock. This result can be found below in Table 6.

Table 6. Mean Emissivity

Star Name	$\epsilon_{H\alpha}$ $erg\,s^{-1}\,cm^{-3}$	$\epsilon_{He\lambda 5876\text{Å}}$ $erg\,s^{-1}\,cm^{-3}$	$\epsilon_{[OIII]}$ $erg\,s^{-1}\,cm^{-3}$
G000.1169-00.5703	1.50e-21	5.32e-23	1.25e-20
ζ Ophiuchi	2.28e-23	5.92e-25	1.09e-20
KGK 2010-10	1.74e-22	5.02e-24	3.36e-20
CPR 2002A37	9.50e-22	2.26e-23	9.54e-19
BD+43 3654	2.10e-21	6.30e-23	2.71e-19
G342.5873+00.1600	3.56e-22	1.26e-23	3.18e-21

NOTE—Mean emissivity of each star. The value given is the average emission in $erg\,s^{-1}\,cm^{-3}$ for the region in the +y axis.

In Table 6, we see that the weakest emissivity is in $HeI\,\lambda 5876$Å, while the strongest is for $[OIII]$. This agrees with Meyer et al. (2014), who found the total $[OIII]$ emission was an order of magnitude higher than hydrogen.

4.5. *Luminosity Visualization*

To verify that the emission profile for each bow shock matches the density plots, we generate images for the $\Lambda_{H\alpha}$, $\Lambda_{He\lambda 5876\text{Å}}$, $\Lambda_{[OIII]}$ cooling emissions of each shock.

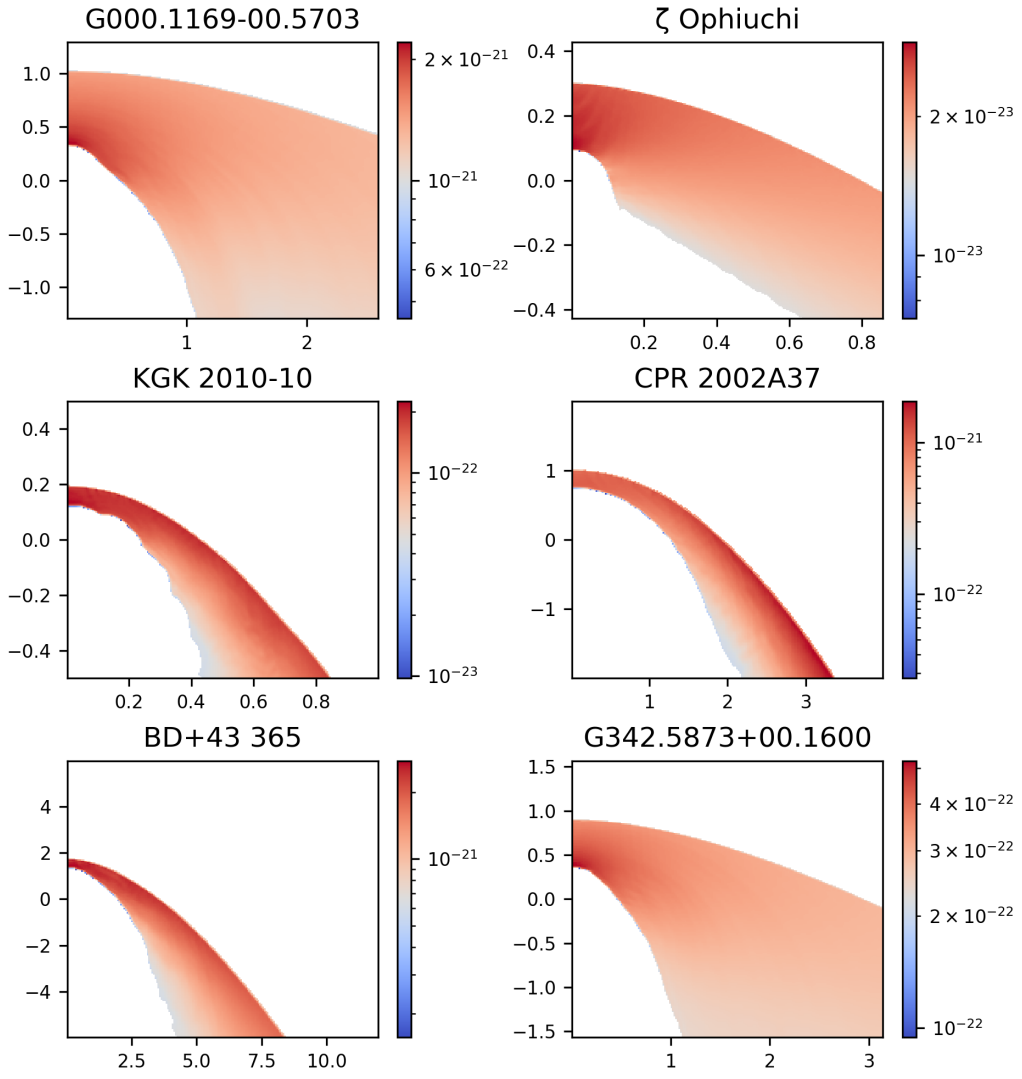

Figure 20. H_α emissivity for each star. The axes are in units of Pc and emissivity is in $erg\,s^{-1}\,cm^{-3}$. The plots are truncated from the full result grid to highlight the bow shock.

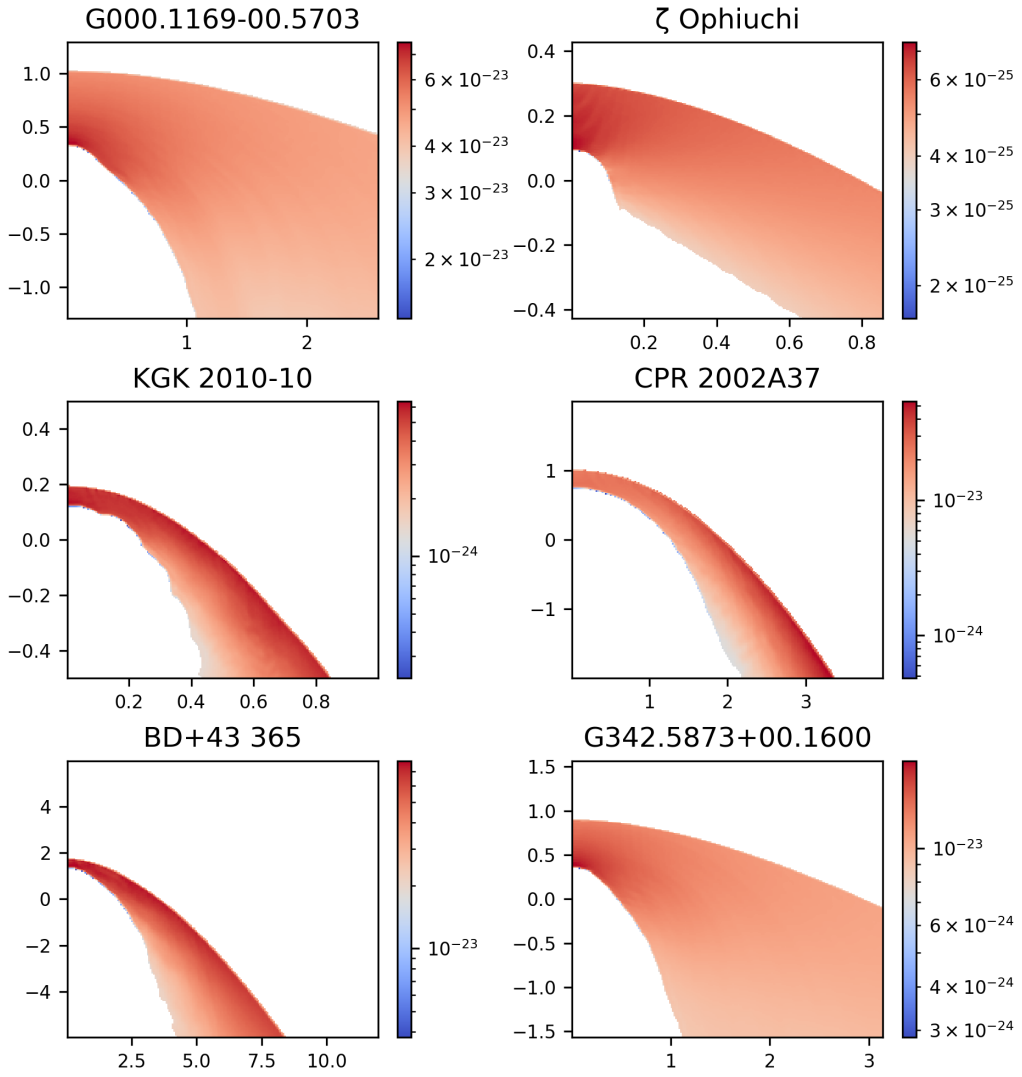

Figure 21. *HeI* λ5876Å emissivity for each star. TThe axes are in units of Pc and emissivity is in $erg\,s^{-1}\,cm^{-3}$. The plots are truncated from the full result grid to highlight the bow shock.

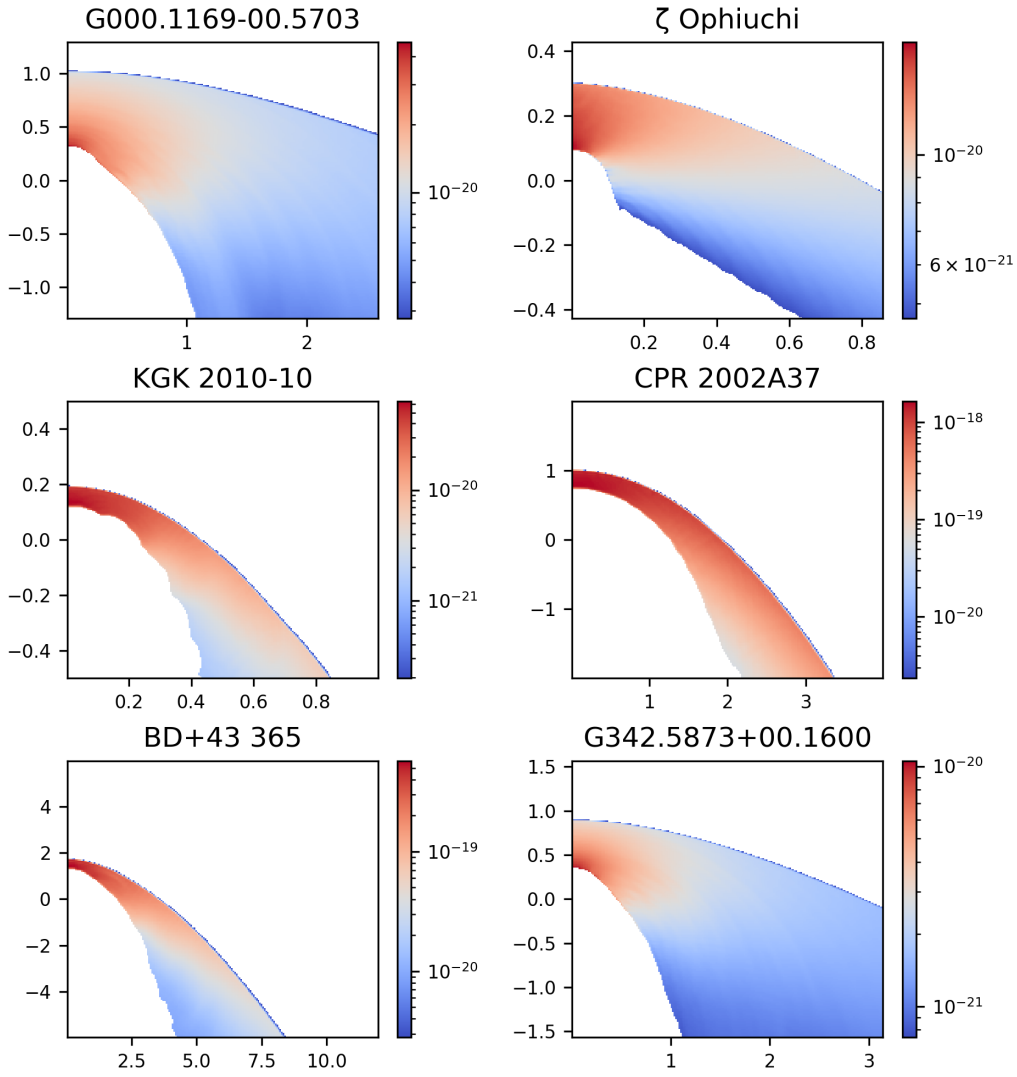

Figure 22. $[OIII]$ emissivity for each star. The axes are in units of Pc and emissivity is in $erg\,s^{-1}\,cm^{-3}$. The plots are truncated from the full result grid to highlight the bow shock.

Looking at the emissions maps, we see that the brightest part of each shock is at the bow shocks front. We can also see in Figures 20 - 22 that, as in Figure 15, the bow shock of ζ Ophiuchi is not nearly as well defined as the other stars. However in these images it is apparent that there is an area of shocked ISM in front of the star, and it has a clearly defined bright spot in front of its direction of travel similar to the other simulations, and WISE observation.

It is also apparent that for the $H\alpha$ and $HeI\,\lambda$5876Å emission of CPR 2002A37, that the brightest spot is on the side of the star, yet its $[OIII]$ emission is still brightest in the front. This confirms the results of Meyer et al. (2014), which found that the $H\alpha$ emission were brightest on the side of a runaway star with a v_* of $70 kms^{-1}$. The ideal result for the $H\alpha$ emission of CPR 2002A37 would be to have its peak emissions in front of the star for simultaneous observation in multiple wavelengths. However, because the shock is not visible opposite the direction of travel in the WISE image, we will find average emissions for the $H\alpha$ and $HeI\,\lambda$5876Å bands in the $y > 0$ region for each star to allow a single image to be taken instead of searching for CPR 2002A37's $H\alpha$ bright spot.

4.6. *Observatory Selection*

Since the runway stars we selected can be found across the celestial sky, we need to select telescopes in both the northern and southern hemisphere. Further the ideal observatories(s) will have an open submission policy. There is one US based observatory meets this selection criteria: The Gemini Observatory, which consists of twin 8.1 meter telescopes. Each telescope of the Gemini Observatory is located in an ideal location for observation: one on Mauna Kea in the northern hemisphere, and one

in the southern hemisphere on the Cerro Pachon mountain in Chile[6]. Since each telescope is the same size and has similar instruments, constructing an observability feasibility study of each bow shock is greatly simplified.

In this feasibility study, we will find the signal to noise ratio (SNR) for specific lines on the Gemini Multi-Object Spectrograph (GMOS) instrument in the visible spectrum using intensities derived from bow shock simulations. This instrument provides the ideal capabilities to observe the $H\alpha$, $HeI\,\lambda 5876$Å, and $[OIII]$ lines, with its $0.36-1.03\mu m$ sensitivity [7]. Both GMOS-N and GMOS-S have nearly identical capabilities[8], therefore a signal to noise estimate for one telescope will be valid for the other. To verify that the bow shocks for each star simulated can be observed in the $H\alpha$, $HeI\,\lambda 5876$Å, and $[OIII]$ emission lines, we will require that the SNR measured exceeds 10 using the GMOS spectrograph.

4.7. *Bow Shock Luminosity*

We measure the luminosity from the emmisivity of the bow shock by first defining a square region for the brightest part of the shock. In Figure 8, the width of each shock in the direction of travel is less than the 5.5 arcminute limit of the GMOS instrrument[9]. We measure the width of the brightest region of a selected stars shock in arcminutes from the WISE image and multiply the width by the stars distance in Table 2 to get its width in Pc. The measured regions are highlighted in Figure 23.

[6] https://www.gemini.edu/about/gemini-telescopes-science-and-technologies
[7] https://www.gemini.edu/instrumentation/gmos
[8] https://www.gemini.edu/instrumentation/gmos
[9] http://www.gemini.edu/sciops/instruments/factsheet

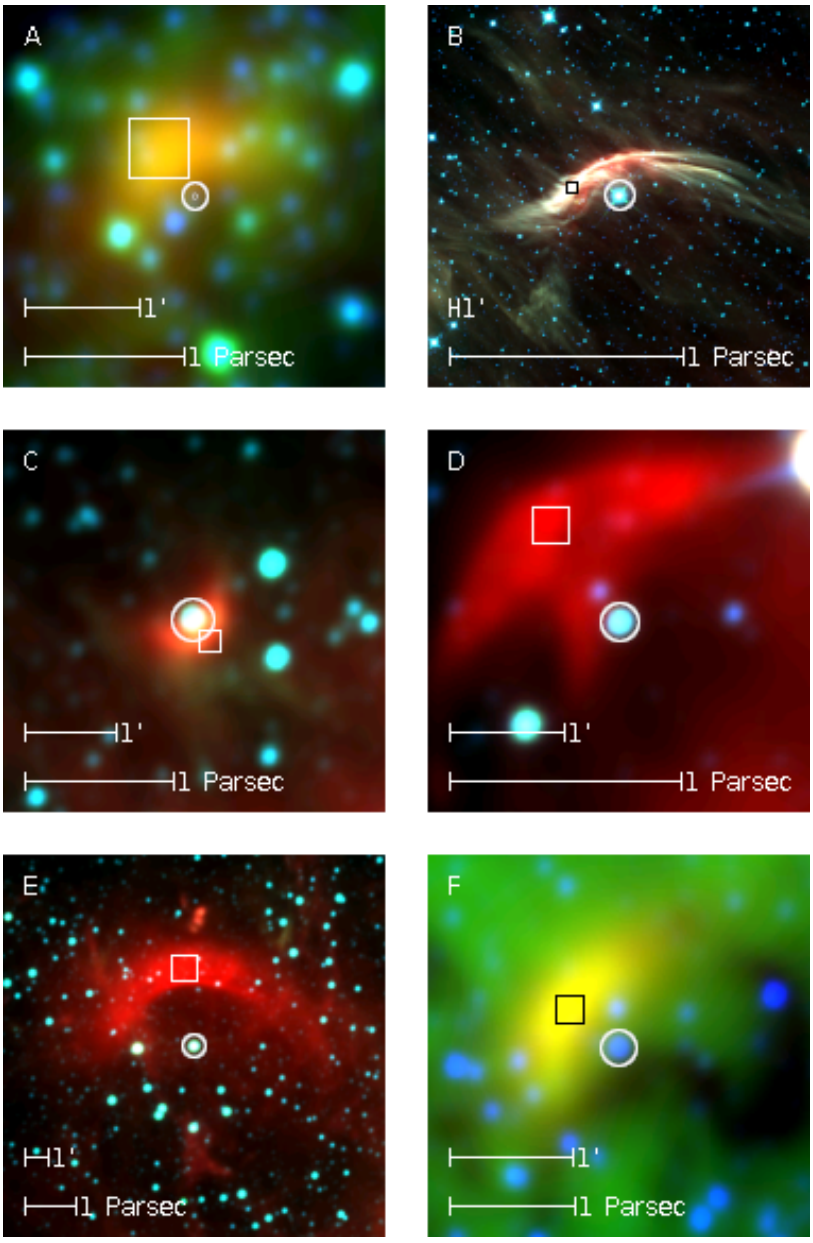

Figure 23. WISE images of selected runaway stars. As in Figure 8, each star is highlighted by a circle, and the selected output region is represented by a square.

In Figure 23, the square represents a 2D slice of the total 3D emission zone defined by the maximum slit width of GMOS. We then multiplied the resulting volume of a shock by its corresponding $\Lambda_{emmisions}$ to get the total luminosity of the brightest region.

Table 7. Output Luminosity

Star Name	Width Arc Min	Width Parsec	$H\alpha$ $erg\,s^{-1}$	$HeI\lambda 5876$Å $erg\,s^{-1}$	$[OIII]$ $erg\,s^{-1}$
G000.1169-00.5703	0.5	0.016	3.17e+28	1.13e+27	2.65e+29
ζ Ophiuchi	1.0	0.500	6.78e+30	1.76e+29	3.25e+33
KGK 2010-10	0.2	0.150	7.22e+30	2.08e+29	1.40e+33
CPR 2002A37	0.3	0.100	7.68e+30	1.82e+29	7.71e+33
BD+43 3654	1.0	0.602	1.13e+33	3.37e+31	1.45e+35
G342.5873+00.1600	0.2	0.186	2.80e+31	9.91e+29	2.51e+32

NOTE—Luminosity of slit region target for each bow shock. The distance used is the same as in Table 2.

In Table 7, the luminosity of BD+43 3654's shock is two orders of magnitude higher than the other bow shocks. Given that the mass of BD+43 3654 is about $20M_{\odot}$ larger than any other simulated star and its observed bow shock is so clearly defined (despite distance of 1577 parsecs), this result is not too surprising.

4.8. *Flux Calculations*

To find the amount of light that reaches the GMOS spectrograph each second we need to calculate to output flux of each line. Because the maximum slit width for

GMOS is 5", we need to scale the output luminosities in Table 7 to the amount emitted by the region that the instrument observes. We calculates the observable flux (f) for each bow shock on the telescope detector using equation 26 below.

$$f = \frac{L}{4\pi d^2} \frac{S_w * S_l}{A} \tag{26}$$

In Equation 26, L is the output luminosity corresponding to the target area from Table 7,S_w is the width of the GMOS slit, S_l is the length of the GMOS slit, A is the area of the bow shock section (in arc seconds), and d is the star's distance (Table 2). Because the slit for GMOS is up to 5.5′ long, we use the width of the bow shock in arc seconds from Table 7 for S_l to constrain the maximum flux.

Table 8. Observable Flux

Star Name	$f_{H\alpha}$ $ergs^{-1}cm^{-2}$	$f_{He\lambda 5876Å}$ $ergs^{-1}cm^{-2}$	$f_{[OIII]}$ $ergs^{-1}cm^{-2}$
G000.1169-00.5703	2.11e-14	7.49e-16	1.77e-13
ζ Ophiuchi	1.95e-14	5.07e-16	9.35e-12
KGK 2010-10	9.04e-15	2.61e-16	1.75e-12
CPR 2002A37	4.92e-14	1.17e-15	4.94e-11
BD+43 3654	2.19e-12	6.57e-14	2.83e-10
G342.5873+00.1600	2.29e-14	8.10e-16	2.05e-13

NOTE—Flux on detector from each bow shock.

In Table 8 the highest simulated flux for each star is in $[OIII]$, while the $HeI\,\lambda$5876Å is lowest. This lines up with the results in Table 7, where $[OIII]$ had the highest luminosity, and $HeI\,\lambda$5876Å had the lowest.

4.9. *Integration Time Calculations*

We used the integration time calculator for GMOS[10] to determine which bow shocks can be detected in the selected lines. To calculate the SNR time we used the following settings: extended source with a uniform surface brightness of 22.0 $mag/arcsec^2$, a single emission line at 6563Å, 5876Å, or 5007Å for $H\alpha$, $HeI\,\lambda$5876Å or $[OIII]$ respectively. the line flux was set to $1.55x10^{-15}\,erg\,s^{-1}\,cm^2$, and a continuum flux density of $1.0x10^{-17}\,erg\,s^{-1}\,cm^2$ Å^{-1}. These settings were chosen because they are the default for the instrument. The minimum line width of 600 kms^{-1} allowed by GMOS, for $[OIII]$ integration, is much larger then the $\sim 5.0\,kms^{-1}$ thermal velocity of the gas. This means that the instrument constrains the maximum resolution of each line observation.

The B600 grating was chosen because of its optimal performance in the visible spectrum compared to the other gratings, and set our central wavelength to 585.0nm, for a focal plane unit with a 5.0" slit. For our detector properties, we used the default setup with 2 pixel spatial binning. We assumed moderate observing conditions which allow 70% image quality, 70% clouds, 50% water vapor, 50% background light and an air-mass of 1.5. Each integration calculation was set up to find the SNR for a specified

[10] http://www.gemini.edu/instrumentation/gmos/exposure-time-estimation

exposure time, and using the optimum SNR ratio analysis method for a sky aperture with a 5x ratio between the sky and target apertures.

For each SNR calculation, we started with the default 900 second integration time. If this did not produce a SNR above 10, we increased the time by until all wavelengths had a SNR greater than 10. The SNR in $H\alpha$ and $[OIII]$ lines is greater than 10 for each bow shock, with the $HeI\,\lambda$5876Å line having the lowest SNR for each shock. Because the SNR ratio for Helium is much lower than the other bands, it is the determining factor on integration time to get each line in one observation.

Only one star, KGK 2010-10, had an SNR below 10, with a SNR of 9. We increased the integration time to 1500 seconds for KGK 2010-10. This resulted in a SNR ratio of 10 for KGK 2010-10.

Table 9. GMOS Integration Time and SNR

Star Name	Integration Time	$H\alpha$	$HeI\,\lambda$5876Å	$[OIII]$
	s	SNR	SNR	SNR
G000.1169-00.5703	900	98	14	244
ζ Ophiuchi	900	94	11	1780
KGK 2010-10	1500	81	10	994
CPR 2002A37	900	151	18	4092
BD+43 3654	900	1016	173	9794
G342.5873+00.1600	900	102	14	263

NOTE—Final recommended integration time, and minimum SNR for each bow shock in $H\alpha$, $HeI\,\lambda$5876Å, and $[OIII]$.

Table 9 gives our final anticipated SNR ratio for the selected integration times. With $t_{exp} > 900s$, $H\alpha$, and $[OIII]$ bands can be expected to have SNR>> 10. this result is not unexpected as observations in $H\alpha$ and $[OIII]$ by van Buren et al. (1995) and Gull & Sofia (1979) respectively used other, smaller telescopes to observe bow shocks in these two wavelengths. Given the high SNR for BD +43 3654, and CPR 2002A37 in $HeI\ \lambda 5876$Å, they would be ideal targets to verify the simulations before attempting to observe the fainter bow shocks simulated. We also also recommend observing ζ Ophiuchi's bow shock despite the stars highly asymmetrical shock because of its proximity to Earth.

5. CONCLUSION

The 2D hydrodynamics simulations we carried out produced results which allow us to determine the observability of runaway star bow shocks using the Gemini telescopes. We used the PLUTO code by Mignone et al. (2007) based on the methodology outlined by Meyer et al. (2014), to produce simulations for six different stars from Kobulnicky et al. (2018b). These simulations gave results that allow us to determine the observability of bow shocks in $H\alpha$, $HeI\,\lambda$5876Å, and $[OIII]$ by the GMOS instrument.

We based our simulations parameters on the six stars selected from Kobulnicky et al. (2018b). Using the methodology outlined by Meyer et al. (2014), we then derived the remaining physical parameters required. The heating and cooling functions were derived separately using the methodology outlined by Meyer et al. (2014). This procedure left us with six sets of well defined parameters to run our simulations.

Each simulation was run for at least 0.5 Myr before we analyzed the results to determine the observability of each bow shock in $H\alpha$, $HeI\,\lambda$5876Å, and $[OIII]$. This analysis was done by removing any un-shocked stellar wind and ISM material from the results before finding the emissivity of the bow shock. We then plotted the resulting emissivity maps of each simulation to verify that the bow shocks structure matched precious work and observations by WISE.

Each emissivity map was then used to derive the luminosity of the brightest part of the bow shock. in doing so we were able to verify that the luminosity for $H\alpha$, and $[OIII]$ were of the same order of magnitude as previous work by Meyer et al. (2014). This allowed us to find the flux of each bow shock in the three selected wavelengths that would be observable by the GMOS instrument of the Gemini Telescopes. After

running the flux values for each emission through the GMOS observation calculator we found the minimum observation time for each shock to be observed in all 3 bands simultaneously.

Our simulations have shown that it is possible to observe the bow shocks of runaway stars in $H\alpha$, $HeI\,\lambda$5876Å, and $[OIII]$ with moderate integration times. The initial targets would be ζ Ophiuchi, CPR 2002A37, and BD +43 3654. CPR 2002A37 and BD +43 3654 have the highest SNR of our simulations which make them ideal for validating the data set. This would then allow the data to be extrapolated to other O class stars. Because ζ Ophiuchi's is the closest runaway star in our data set to Earth, and has a long straight bow shock it would also be a an ideal candidate for initial observation. This would allow for insights into expanding the data set to include runway stars with asymmetrical bow shocks. Simultaneously this would allow for fainter runaway star fluxes to be calculated through further simulation refinement. By expanding the data set to allow for a much larger range of M_* than our initial study, an ISM composition survey through runaway bow shock spectroscopy could be accomplished out using spectroscopy of runaway stars around the Galaxy.

"This research has made use of the NASA/IPAC Infrared Science Archive, which is funded by the National Aeronautics and Space Administration and operated by the California Institute of Technology."

Facility: IRSA, WISE

We would like to give special thanks to Dr. Meyer for his help and contributions to the project.

Software: PLUTO (Mignone et al. 2007)

REFERENCES

Asplund, M., Grevesse, N., Sauval, A. J., & Scott, P. 2009, ARA&A, 47, 481, doi: 10.1146/annurev.astro.46.060407.145222

Baker, J. G., & Menzel, D. H. 1938, ApJ, 88, 52, doi: 10.1086/143959

Batchelor, G. K. 2000, An Introduction to Fluid Dynamics

Blaauw, A. 1961, BAN, 15, 265

Brown, D., & Bomans, D. J. 2005, A&A, 439, 183, doi: 10.1051/0004-6361:20041054

Brown, W. R. 2015, ARA&A, 53, 15, doi: 10.1146/annurev-astro-082214-122230

Comeron, F., & Kaper, L. 1998, A&A, 338, 273

Eldridge, J. J., Genet, F., Daigne, F., & Mochkovitch, R. 2006, MNRAS, 367, 186, doi: 10.1111/j.1365-2966.2005.09938.x

Godunov, S. K., & Bohachevsky, I. 1959, Matematičeskij sbornik, 47(89), 271

Green, S., Mackey, J., Kavanagh, P., et al. 2022, arXiv e-prints, arXiv:2203.06331. https://arxiv.org/abs/2203.06331

Gull, T. R., & Sofia, S. 1979, ApJ, 230, 782, doi: 10.1086/157137

Harten, A., Lax, P. D., & Leer, B. v. 1983, SIAM Review, 25, 35, doi: 10.1137/1025002

Henney, W. J., Arthur, S. J., de Colle, F., & Mellema, G. 2009, MNRAS, 398, 157, doi: 10.1111/j.1365-2966.2009.15153.x

Hoogerwerf, R., de Bruijne, J. H. J., & de Zeeuw, P. T. 2000, ApJL, 544, L133, doi: 10.1086/317315

—. 2001, A&A, 365, 49, doi: 10.1051/0004-6361:20000014

Hummer, D. G. 1994, MNRAS, 268, 109, doi: 10.1093/mnras/268.1.109

Kobulnicky, H. A., Chick, W. T., & Povich, M. S. 2018a, ApJ, 856, 74, doi: 10.3847/1538-4357/aab3e0

—. 2019a, AJ, 158, 73, doi: 10.3847/1538-3881/ab2716

—. 2019b, VizieR Online Data Catalog, J/AJ/158/73

Kobulnicky, H. A., Schurhammer, D. P., Baldwin, D. J., et al. 2018b, VizieR Online Data Catalog, J/AJ/154/201

Kobulnicky, H. A., Chick, W. T., Schurhammer, D. P., et al. 2016, ApJS, 227, 18, doi: 10.3847/0067-0049/227/2/18

Meyer, D. M. A., Mackey, J., Langer, N., et al. 2014, MNRAS, 444, 2754, doi: 10.1093/mnras/stu1629

Meyer, D. M. A., Mignone, A., Petrov, M., et al. 2021, MNRAS, 506, 5170, doi: 10.1093/mnras/stab2026

Meyer, D. M. A., van Marle, A. J., Kuiper, R., & Kley, W. 2016, MNRAS, 459, 1146, doi: 10.1093/mnras/stw651

Mignone, A. 2014, Journal of Computational Physics, 270, 784, doi: 10.1016/j.jcp.2014.04.001

Mignone, A., Bodo, G., Massaglia, S., et al. 2007, ApJS, 170, 228, doi: 10.1086/513316

Mohamed, S., Mackey, J., & Langer, N. 2012, A&A, 541, A1, doi: 10.1051/0004-6361/201118002

Osterbrock, D. E. 1989, Astrophysics of gaseous nebulae and active galactic nuclei

Poveda, A., Ruiz, J., & Allen, C. 1967, Boletin de los Observatorios Tonantzintla y Tacubaya, 4, 86

Spitzer, L. 1978, Physical processes in the interstellar medium, doi: 10.1002/9783527617722

van Buren, D., Noriega-Crespo, A., & Dgani, R. 1995, AJ, 110, 2914, doi: 10.1086/117739

Wiersma, R. P. C., Schaye, J., & Smith, B. D. 2009, MNRAS, 393, 99, doi: 10.1111/j.1365-2966.2008.14191.x

Wilkin, F. P. 1996, ApJL, 459, L31, doi: 10.1086/309939